

Flying electron spin control gates

Paul L. J. Helgers,^{1,2} James A. H. Stotz,^{1,3,*} Haruki Sanada,² Yoji Kunihashi,² Klaus Biermann,¹ and Paulo V. Santos^{1,†}

¹*Paul-Drude-Institut für Festkörperelektronik, Leibniz-Institut im Forschungsverbund Berlin e.V., Hausvogteiplatz 5-7, 10117 Berlin, Germany*

²*NTT Basic Research Laboratories, NTT Corporation,*

3-1 Morinosato-Wakamiya, Atsugi, Kanagawa 243-0198, Japan

³*Department of Physics, Engineering Physics & Astronomy, Queen's University, Kingston, ON, K7L3N6 Canada*

(Dated: November 23, 2021)

The control of "flying" (or moving) spin qubits is an important functionality for the manipulation and exchange of quantum information between remote locations on a chip. Typically, gates based on electric or magnetic fields provide the necessary perturbation for their control either globally or at well-defined locations. Here, we demonstrate the dynamic control of moving electron spins via contactless gates that move together with the spin. The concept is realized using electron spins trapped and transported by moving potential dots defined by a surface acoustic wave (SAW). The SAW strain at the electron trapping site, which is set by the SAW amplitude, acts as a contactless, tunable gate that controls the precession frequency of the flying spins via the spin-orbit interaction. We show that the degree of precession control in moving dots exceeds previously reported results for unconstrained transport by an order of magnitude and is well accounted for by a theoretical model for the strain contribution to the spin-orbit interaction. This flying spin gate permits the realization of an acoustically driven optical polarization modulator based on electron spin transport, a key element for on-chip spin information processing with a photonic interface.

I. INTRODUCTION

The spin field-effect transistor proposed by *Datta and Das* [1] relies on the precession of moving (or flying) electron spins around the effective magnetic field $\vec{B}_{\text{SO}}(\mathbf{k})$ associated with the spin-orbit (SO) interaction, which depends on electron momentum $\hbar\mathbf{k}$. \vec{B}_{SO} can be electrically controlled by an electrostatic gate via the Bychkov-Rashba effect,[2] thus opening the way for dynamic spin manipulation by electric fields. Spin transistors based on the electrical spin control have so far been demonstrated only for ballistic spin transport along short ($< 2 \mu\text{m}$) channels [3, 4].

SO-based spin control over long transport distances, which normally takes place in the diffusive regime, faces two main challenges. The first is D'yakonov-Perel' (DP) spin dephasing[5] associated with the momentum-dependence of \vec{B}_{SO} . Approaches to reduce DP spin dephasing and enable long-range spin transport lengths (ℓ_s) include the engineering the SO interaction [6–11] as well as exploitation of motional narrowing effects [5]. The latter takes advantage of the inverse dependence of the DP dephasing rate on the carrier scattering time, which can be achieved via increased momentum scattering by impurities [12] or at the boundaries of narrow transport channels (i.e., channel widths less than the precession period, L_{SO} under \vec{B}_{SO}). This latter approach has been realized using quantum wire channels [13, 14] as well as by enclosing the spins within moving potential dots [15, 16].

The second major challenge for spin control is to devise field configurations to simultaneously drive spin motion and generate a tunable \vec{B}_{SO} for controlled spin precession. An elegant solution is offered by the carrier transport by moving potential dots produced by a surface acoustic wave (SAW) along a one-dimensional (1D) channel. Figure 1 depicts an example based on a quantum wire (QWR) transport channel. Here, the moving piezoelectric potential modulation produced by the SAW stores photo-excited electrons and holes at different SAW subcycles and transports them with the acoustic velocity. The spatial separation of electrons and holes prevents recombination [17] and, simultaneously, also suppresses spin relaxation due to the electron-hole exchange interaction [18]. The ambipolar SAW transport can thus transfer electron spins over long distances (up to $100 \mu\text{m}$) while enabling optical spin readout by detecting the polarization of photons emitted by the recombination of the transported carriers [16, 19–22].

Concomitantly with the transport, the SAW strain [23–27] and piezoelectric fields at the carrier location induce a \vec{B}_{SO} contribution, which moves congruently with the carriers [cf. Fig. 1]. The SAW amplitude acts, therefore, as a contactless, flying spin gate, which dynamically controls the rate of spin precession during transport. In this work, we demonstrate that long-range acoustic transport can be combined with a high degree of dynamical control of the spin precession rate (by over 250%) if the flying spins are transported while confined within micron-sized moving potential dots. This degree of precession control exceeds by over an order of magnitude previous results for acoustic transport in 2D quantum well (QW) channels [21, 28]. We also show

* jstotz@queensu.ca

† santos@pdi-berlin.de

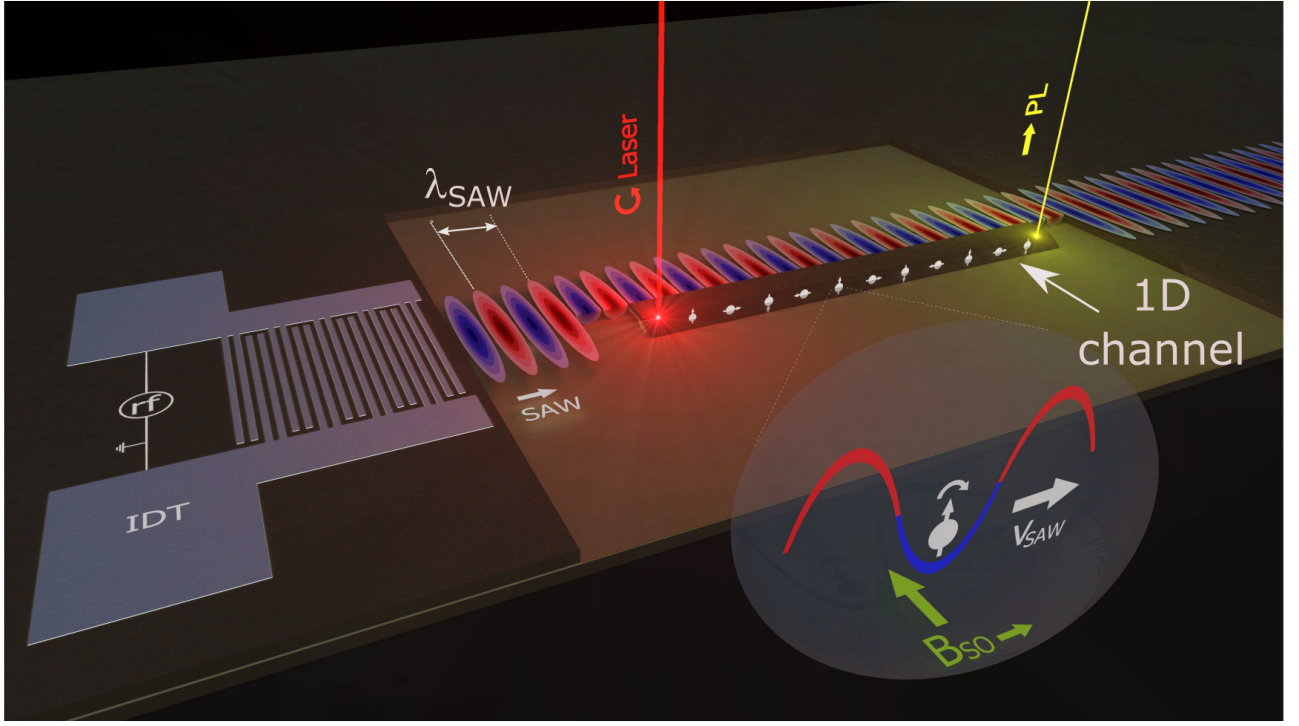


FIG. 1. **Flying control gate for electron spins.** A surface acoustic wave (SAW) excited by an interdigital acoustic transducer (IDT) is applied along a quasi-one dimensional (1D) semiconductor channel. The piezoelectric potential of the SAW creates a moving quasi-zero dimensional (0D) potential dot, which captures spin-polarized, photoexcited electrons and holes and transports them along the channel with the SAW velocity. Simultaneously, the SAW strain field induces an effective spin-orbit magnetic field B_{SO} at the carrier transport sites with amplitude proportional to the SAW field. The latter acts as a flying spin gate to control the spin precession rate.

that the precession rate is mainly mediated by the acoustic strain imparted by the SAW in the storage phase of the electron spins during transport. The latter essentially enables the carrier wave to also act as a flying spin gate controlled by the SAW amplitude.

The study addresses two types of acoustically defined, moving potential dots. In one system, the dots are formed by propagating a SAW along a quasi-planar GaAs quantum wire (QWR) [as illustrated in Fig. 1]. We have also investigated spin transport and manipulation in moving potential dots created by the interfering piezoelectric fields of orthogonal SAW beams (denoted as dynamic quantum dots, DQDs[15, 29]). For both types of moving dots, we experimentally demonstrate the flying spin gates using optically excited spins that can be acoustically transported over large distances (tens of microns) with the spin precession rate controlled over a wide dynamic range dictated by the SAW amplitude (Sec. II) and, notably, without external electric or magnetic fields. The measured precession rates are well accounted for by an analytical model for the SO fields generated by the SAW strain and piezoelectric fields, from which the strain-related SO parameters can be experimentally determined (Sec. II). As a further check of consistency, we show that spin precession rates and their dependence on the acoustic fields are also in good agreement with microscopic calculations of the spin splittings under the SAW field using a tight-binding approach. Interestingly, while the moving dot geometry enables precession control, a substantial enhancement of the spin lifetime due to motional narrowing is only observed for the DQDs. The limited spin lifetimes in the QWRs, in contrast, is attributed to the fact that the positive impact of lateral confinement on the spin lifetime is offset by spin scattering at the lateral, compositional interfaces. Even so, the dramatic ability of the flying spin gates to control the precession frequency by the SAW amplitude demonstrates a processor for optically encoded polarization information based on the dynamic control of electron spins during acoustic transport.

II. RESULTS

Acoustic spin transport

The structure of the QWR samples is illustrated in Fig. 2(a). As described in the Methods section, the GaAs QWRs are fabricated by combining steps of surface patterning and overgrowth by molecular beam epitaxy (MBE). In this process, the growth of an (Al,Ga)As/GaAs/(Al,Ga)As QW stack over a patterned ridge leads to the formation of a thicker GaAs region (the

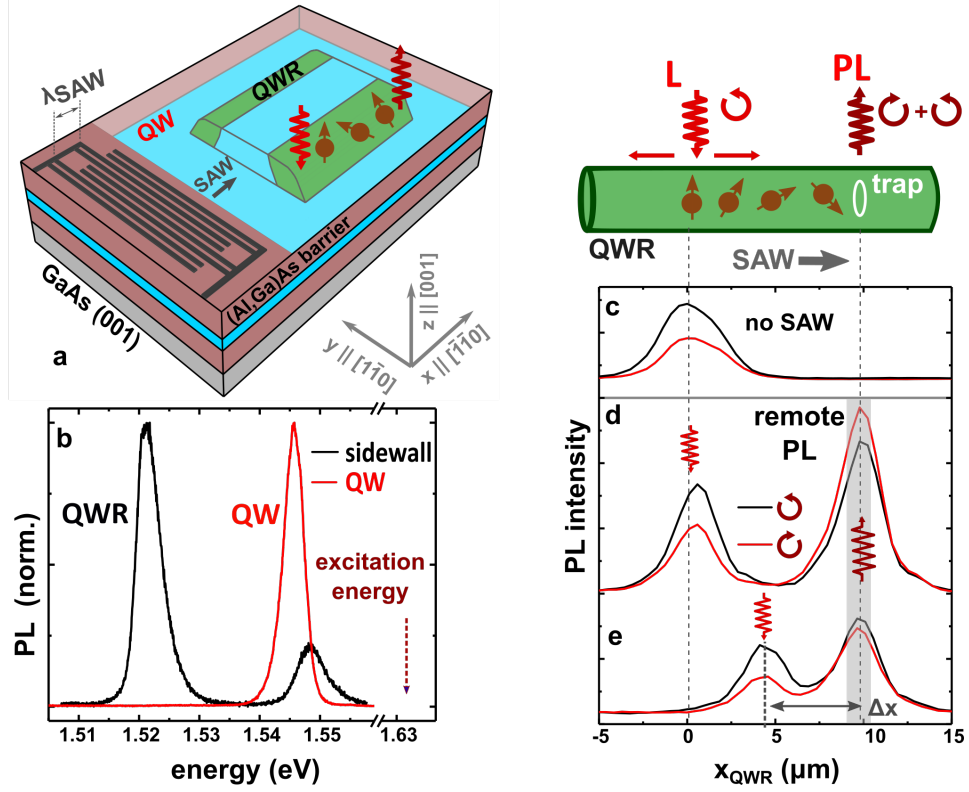


FIG. 2. **Optically detected transport of spins in planar quantum wires.** (a) Sidewall quantum wires (QWRs) formed by the epitaxial overgrowth of a quantum well (QW) on a GaAs (001) substrate structured with shallow ridges [30]. Photoexcited carriers are transported along the QWR by surface acoustic waves (SAWs) generated by interdigital acoustic transducers (IDTs). (b) Photoluminescence (PL) spectra recorded outside (red) and on (black) a ridge sidewall showing the emission lines of the QW (1.548 eV) and QWR (1.521 eV), respectively. (c)-(e) Profiles of the right (black) and left (red) circularly polarized PL along the QWR axis (x_{QWR} coordinate) recorded under the configuration illustrated in the upper panel (c) in the absence and (d)-(e) under a SAW. The PL was excited by a right-circularly polarized laser spot focused at $x_{\text{QWR}} = 0$ for (c) and (d), and at $x_{\text{QWR}} = 4.5 \mu\text{m}$ for (e).

QWR) at the ridge sidewalls, which is electrically connected to the QW[30]. The photoluminescence features of the sample are summarized in Fig. 2(b). Here, the red and black curves compare PL spectra recorded under confocal excitation and detection on the QW region and on the ridge sidewall (corresponding to the QWR position), respectively. The former shows a single PL line with a linewidth (full-width-at-half-maximum, FWHM) of 4 meV associated with the electron-heavy hole QW exciton at 1.546 eV. The spectrum recorded on the ridge sidewall shows the excitonic emission from the QWR at 1.521 eV with a FWHM of 4.6 meV together with a second line at 1.548 eV (FWHM of 5.4 meV). The latter stems from the QW regions near the QWR, which are slightly thinner than those further from the ridge sidewalls [30]. The energy difference between these two lines yields a lateral confinement energy for electrons (holes) in the QWR of approximately 22 meV (4 meV).

The optical detection of acoustically driven spin transport along the QWR is illustrated in Figs. 2(c)-(e). The experiments were carried out using the geometry depicted in the upper right panel by exciting spins using a right-hand circularly polarized laser beam with energy below the QW resonance. The black and red profiles display the spatial distribution of the integrated PL from the QWR [detection window from 1.517 eV to 1.526 eV, cf. Fig. 2(a)] with right- and left-hand circular polarizations, respectively. In the absence of a SAW [Fig. 2(c)], the emission is restricted to the regions around the excitation spot and has a net right-hand circular polarization. The PL profiles can be fitted with a Gaussian characterized by a FWHM of $4 \mu\text{m}$. The increased spatial PL spread compared to the size of the laser spot is attributed to the diffusion of the spin polarized carriers along the QWR axis.

Figures 2(d) and 2(e) display the corresponding profiles acquired in the presence of a SAW that captures the spin polarized carriers and transports them to trap centers at $x_{\text{QWR}} = 10 \mu\text{m}$, where the electrons and holes recombine. The trapping and recombination centers are defect regions along the QWR[30]. The trapping mechanism, which leads to emission at the same energy as the QWR, is attributed to carrier capture at centers at the interface between the QW (or QWR) layer and the (Al,Ga)As barrier layers assisted by the transverse component of the SAW piezoelectric field, F_z [30, 31]. These centers can capture carriers of one polarity during one half-cycle of the SAW and release them during the passage of carriers of the opposite polarity in the subsequent SAW half-cycle when F_z reverses its sign. The centers provide efficient recombination centers to stop the transport

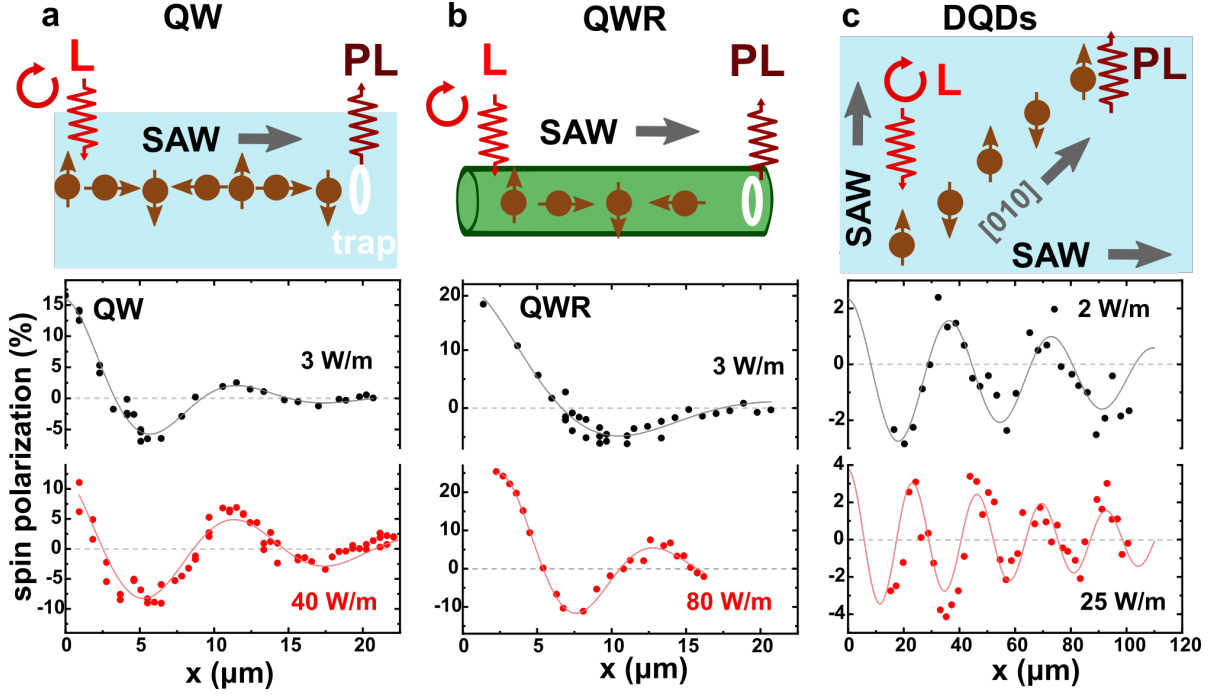


FIG. 3. **Acoustic control of the precession rate of moving spins.** Spin polarization, ρ_s , during transport along (a) a quantum well (QW, excitation wavelength $\lambda_L = 776$ nm, $P_{exc} = 15$ μ W, 20 K), (b) a quantum wire (QWR, $\lambda_L = 776$ nm, $P_{exc} = 30$ μ W (3 W m^{-1}) and $P_{exc} = 150$ μ W (80 W m^{-1}), 20 K), and (c) dynamic dots (DQDs, $\lambda_L = 776$ nm, 12 K). The upper panels illustrate the experimental setup: spin-polarized electrons (brown) are optically injected by a circularly polarized laser (L , red) and transported by a SAW along the $[110]$ direction (QW and QWR) or along the $[010]$ direction (dynamic dots). The curves correspond to different SAW powers P_{SAW} .

and monitor the PL polarization. Note that the PL polarization depends on the transport distance Δx changing from right-[Fig. 2(e)] to left-hand circular polarization [Fig. 2(d)] as Δx increases from 5 to 10 μ m. This is due to the larger precession angle under the SO field accumulated while travelling a longer distance.

Spin precession control

The procedure depicted in Figs. 2(c)-(e) was applied to determine the spatial dependence of the spin polarization ρ_s on the SAW amplitude. The panels of Fig. 3 summarize ρ_s profiles for acoustic transport in three geometries, which are illustrated in the corresponding upper panels: (a) along the QW, (b) along the QWR and (c) using DQDs. For the QW and QWR, the transport distance x is along the $[110]$ -direction, but it is along the $[010]$ -direction for the DQDs. In all cases, ρ_s oscillates with a period that reduces with increasing SAW amplitudes, which demonstrates the operation principle of the acoustic spin gate. In particular, a distinct reversal of the spin polarization can be observed for both the QWR ($x = 12.5$ μ m) and DQD ($x = 25$ μ m) geometries, with the latter occurring well within the spin coherence length of transport.

The solid lines are fits of the experimental data to an exponentially decaying cosine function of the form

$$\rho_s(x) = \rho_s(0) \cos\left(\frac{\Omega_{SO}}{v_{SAW}} \Delta x\right) e^{-\Delta x/\ell_s}. \quad (1)$$

The fit parameters are the total SO angular precession frequency Ω_{SO} as well as the characteristic spin transport length ℓ_s . Ω_{SO} can be expressed in terms of the oscillation period $L_{SO} = 2\pi v_{SAW}/\Omega_{SO}$. The fit parameters ℓ_s and Ω_{SO} are displayed as filled symbols in Fig. 4 as a function of the SAW amplitude (stated in terms of the amplitude of the uniaxial strain component $u_{xx,0} \propto \sqrt{P_{SAW}}$, see definition below). For the QWR (solid red dots), $\ell_s \sim 7$ μ m is independent of the SAW amplitude, and this value is equal to the one measured in the absence of a SAW[32]. In contrast, ℓ_s for the QW (solid black squares) increases with SAW power [cf. Fig. 4(a)]—a behaviour which will be further addressed below. For the DQDs (solid green triangles), ℓ is considerably larger and comparable to the maximum measured transport distance.

A further remarkable result is the strong dependence of Ω_{SO} on the SAW amplitude [cf. Fig. 4(b)] for transport both along the QWRs and by DQDs. These structures thus act as acoustically controlled spin logic and polarization modulators, where the gate is determined by the acoustic amplitude. Their behaviour contrasts with that of the QW data as well as with previous acoustic

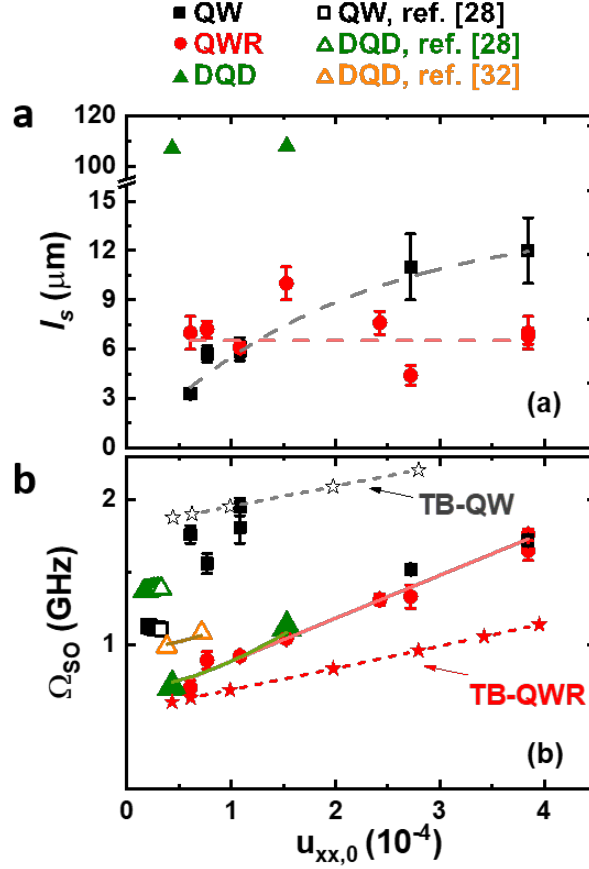


FIG. 4. **Spin dynamics under acoustic fields.** (a) Spin transport length, ℓ_s , and (b) angular precession frequency, Ω_{SO} , as a function of the strain amplitude $u_{xx,0}$ for transport along the QW (black solid squares), QWR (red solid dots), and DQDs on a 30 nm QW (green solid triangles). The orange triangles are for DQDs in a 20 nm-thick QW [28]. The open symbols display data for transport by a single SAW (open squares) and by DQDs (open triangles) in a 20 nm thick QW[21]. Note that the Ω_{SO} is scaled for the DQD data to account for the higher velocity. The open and solid \star 's yield the Ω_{SO} obtained from tight-binding (TB) calculations for the studied QWs and QWRs, respectively. The dashed lines in (a) and (b) are a guide to the eye. The solid red and green lines in (b) are fits to Eqs. (2) and (3) of the QWR and DQD data, respectively.

transport studies of QWs and DQD on thinner QWs (open symbols in Fig. 4 [21, 29]), where the SAW-induced changes in Ω_{SO} are typically less than 10%.

SAW-related spin-orbit fields

In order to quantify the SO fields induced by the SAW, we first note that the strain field of a Rayleigh SAW along $\hat{\mathbf{x}}||[110]$ consists of two uniaxial strain components $u_{xx} = u_{xx,0} \cos(\phi_{SAW})$ and $u_{zz} = u_{zz,0} \cos(\phi_{SAW})$ as well as a phase-shifted shear component $u_{xz} = u_{xz,0} \sin(\phi_{SAW})$ [33]. Here, $\hat{\mathbf{z}}||[001]$ is the QW growth axis, $\phi_{SAW} = (k_{SAW}x - \omega_{SAW}t)$ is the SAW phase, and $k_{SAW} = 2\pi/\lambda_{SAW}$ and ω_{SAW} are the SAW wave vector and angular frequency, respectively. During transport, the SAW piezoelectric potential $\Phi_{SAW} = \Phi_{SAW,0} \cos(\phi_{SAW})$ captures electrons around the SAW phase $\phi_{SAW} = 0$ [cf. Fig. 5(a)] with a strain field $(u_{xx} + u_{zz})$, where they are also subjected to a transverse piezoelectric field F_z proportional to u_{xx} [34].

The lateral dimensions of the QWRs and DQDs are much larger than the QWR (or QW) thickness. For the determination of the Ω_{SO} in QWRs and DQDs, we will neglect the role of the lateral confinement (and of the lateral interfaces) and assume that Ω_{SO} is essentially equal to the one in a QW of the same thickness. We now address the different SO mechanisms acting on spins acoustically transported along the x -direction of a QW with the SAW velocity v_{SAW} . The effective electron wave vector $k_x = m^* v_{SAW}/\hbar$ is determined by the effective electron mass m^* (\hbar is the reduced Planck's constant) [35]. The bulk inversion asymmetry (BIA) of the III-V lattice induces an intrinsic SO field (the Dresselhaus term [36]), which leads to the precession of the moving spins with an angular frequency $\hbar\Omega_D \sim \gamma k_x (\pi/w_z)^2$. Here, w_z denotes the extension of the electron wave function

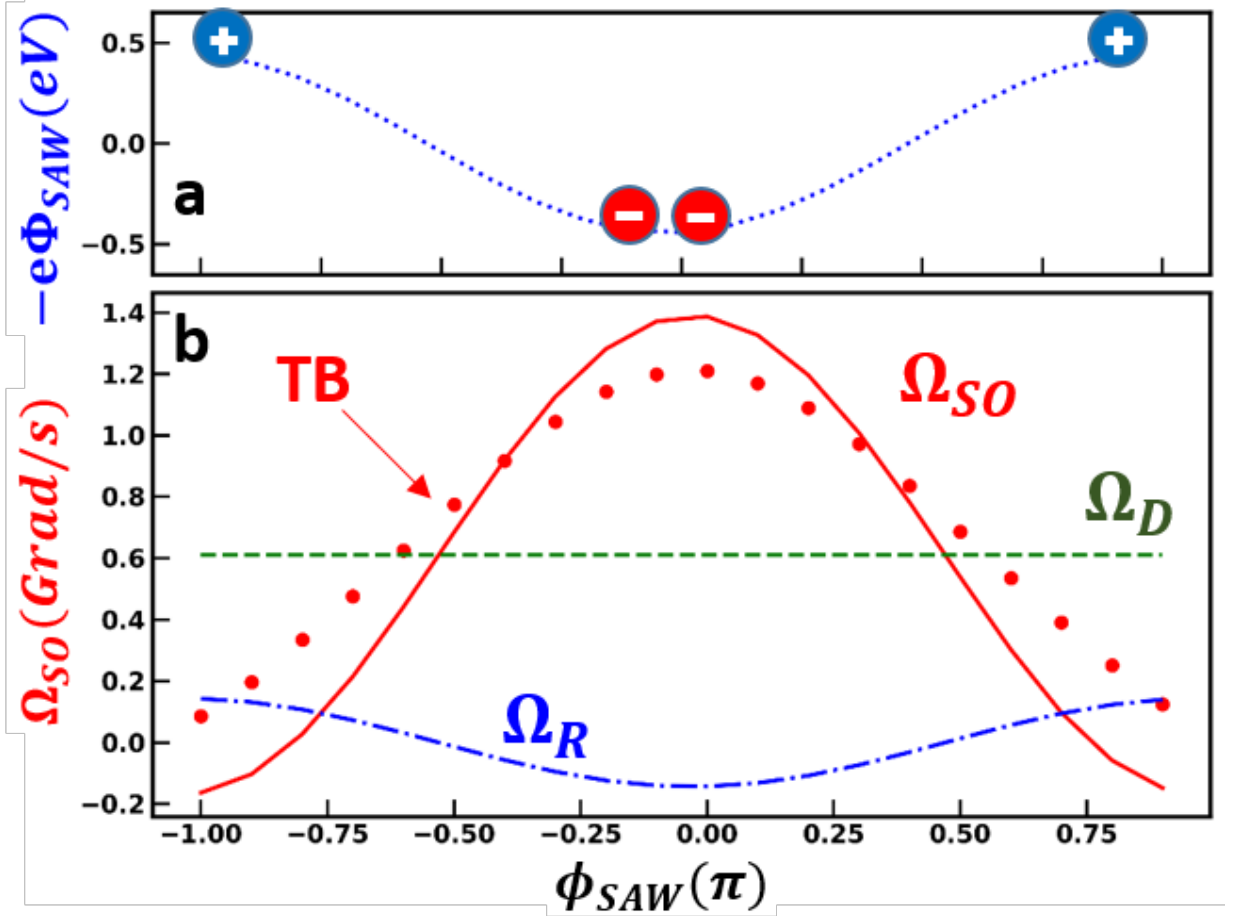


FIG. 5. **Tight-binding calculations of the spin precession rate.** SAW phase (ϕ_{SAW}) dependence of the (a) electronic piezoelectric energy, $-e\Phi_{\text{SAW}}$, and of the (b) electron-spin precession frequency determined by the tight-binding approach for a QW with the same thickness as the QWR under $P_{\text{SAW}} = 100$ W/m. The dashed (Ω_D) and solid lines (Ω_R) are the corresponding Dresselhaus and piezoelectrically induced Rashba contributions, respectively, obtained from Eq. (2).

along z . The structural inversion asymmetry (SIA) induced by the SAW gives rise to precession components related to the strain field, $\hbar\Omega_S = \frac{1}{2}C_3u_{xx}k_x$ [20], as well as to piezoelectric field F_z , $\hbar\Omega_R = 2r_{41}F_zk_x$. The terms γ , r_{41} , and C_3 are material parameters quantifying the strength of the different SO contributions (cf. Sec. SM3). The previous expressions can be combined such that the spin precession frequency for transport by a single SAW beam ($\Omega_{\text{SO}}^{(QW)}$) and by DQDs ($\Omega_{\text{SO}}^{(DQD)}$) can be stated as: [20, 21]

$$\Omega_{\text{SO}}^{(QW)} = \Omega_D \hat{\mathbf{y}} - (\Omega_R + \Omega_S) \hat{\mathbf{y}} \quad (2)$$

$$\Omega_{\text{SO}}^{(DQD)} = \sqrt{2}\Omega_D \hat{\mathbf{x}}' - 2(\Omega_R + \Omega_S) \hat{\mathbf{y}}' \quad (3)$$

In Eq. (3), $\hat{\mathbf{x}}' = \mathbf{x} - \mathbf{y}$ and $\hat{\mathbf{y}}' = \mathbf{x} + \mathbf{y}$ are the unit vectors parallel and perpendicular to the DQD propagation while Ω_R and Ω_S refer to precession frequencies for a single SAW beam along $\hat{\mathbf{x}}$. The $\sqrt{2}$ term in this equation arises from the fact that the propagation velocity of the DQDs equals to the vector sum of the velocities of the individual SAW beams.

Since $F_z \propto u_{xx}$ (hence $\Omega_R \propto \Omega_S$), Eq. (2) predicts a linear dependence of $\Omega_{\text{SO}}^{(QW)}$ on the SAW amplitude. For a quantitative comparison, we first note that while the $\gamma = (17 \pm 2) \times 10^{-30}$ eV m³ [29] and $r_{41} = -(59 \pm 7) \times 10^{-21}$ e m² [20] have well-established values, the reported values of the strain-related parameter C_3 span a wide range (e.g., from 0.81 eV nm in n-type doped bulk GaAs [24, 26] to 0.31 eV nm in a GaAs(001) QW [27]).

The red solid line in Fig. 4(b) is a fit of the QWR data to Eq. (2) and is then used to determine $C_3 = (-2.6 \pm 0.1)$ eV nm (details in Sec. SM5). While larger than previously reported values, this C_3 value reproduces very well the measured data for DQDs (after considering the scaling of Ω_{SO} due to the larger v_{DQD}) and shows more reasonable agreement with the dashed lines in Fig. 4(b) from tight-binding calculations. The relative signs of the terms of Eq. (2) is also consistent with the distinctive slope

of the red solid line in Fig. 4(b). These terms assumed that the electron spins were experiencing the maximum Ω_{SO} as calculated in Fig. 5(b), which supports the assumption that the electrons have a phase purity near $\phi_{\text{SAW}} = 0$.

Tight-binding calculations of the spin splittings

In order to verify the predictions of the analytical model, we have also calculated the SO field Ω_{SO} in QWs using the tight-binding (TB) method [37, 38]. The dots in Fig. 5(b) display the Ω_{SO} dependence on ϕ_{SAW} calculated for the QWR under $P_{\text{SAW}} = 100$ W/m. In the TB calculations, the QWRs were modelled as a thicker QW, thus neglecting the effects of the weak lateral confinement. The total SO component Ω_{SO} oscillates around an average value Ω_D following the harmonic dependence of the SAW fields. To compare with the experiments, we further assume that the electrons are stored around the phases $\phi_{\text{SAW}} = 0$ of minimum electronic piezoelectric energy $-\epsilon\Phi_{\text{SAW}}$, as illustrated in Fig. 5(a). The SAW amplitude dependence of Ω_{SO} at these phases calculated by the TB method is displayed by the \star 's in Fig. 4(b) for the QWR and QW widths. The calculated linear dependence of Ω_{SO} on strain amplitude, which corresponds to the parameter C_3 in Eq.(2), does not depend on the thickness of the structures and is, thus, similar for the QW and QWR. The sign of the C_3 parameter determined by the TB method agrees with the experiments, thus reproducing the increase of the precession rate with SAW amplitude. Its magnitude $|C_3| = 1.65$ eVnm is slightly (33%) smaller than the experimentally determined one, but still well above previously published experimental values.

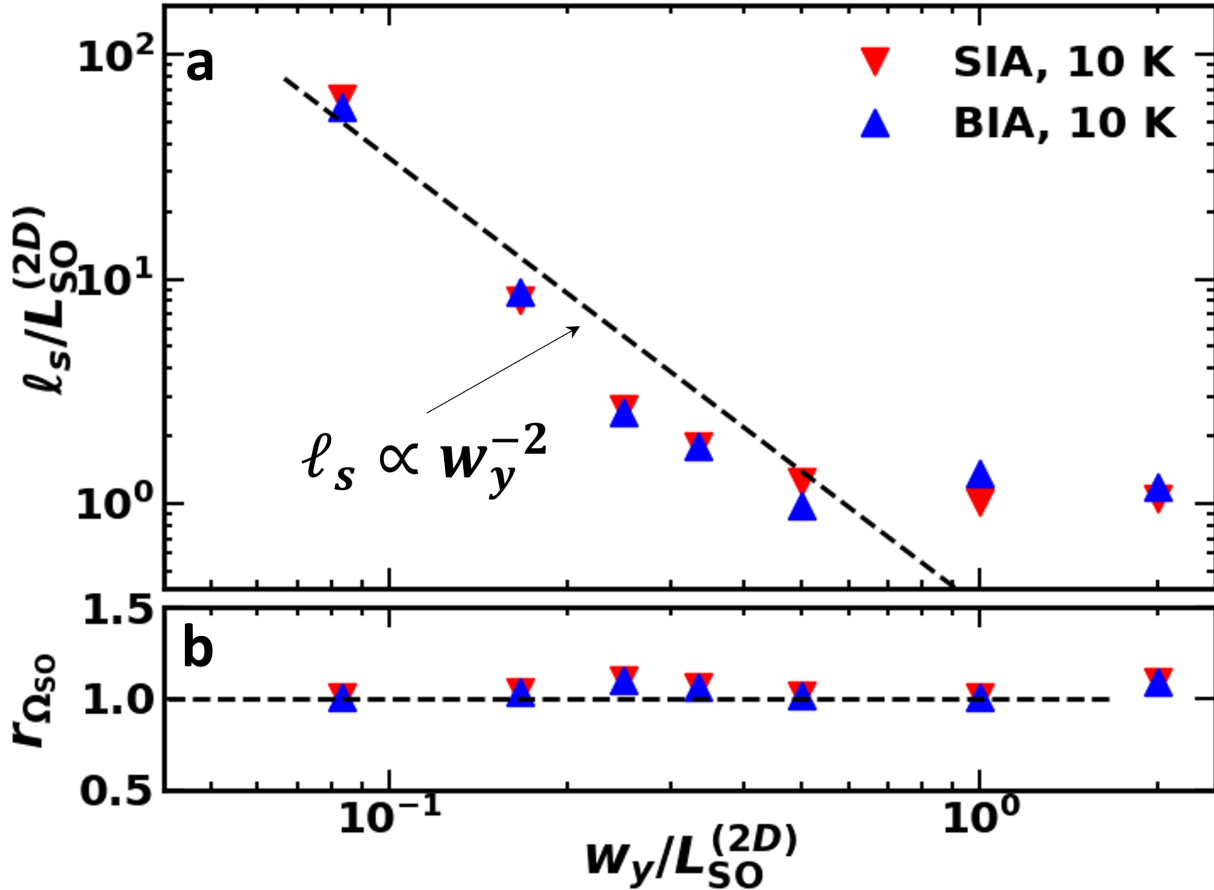


FIG. 6. **Dimensionality effects on spin dephasing.** (a) Spin transport length, ℓ_s , and (b) precession frequency ratio $r_{\Omega_{\text{SO}}} = \Omega_{\text{SO}}(w_y)/\Omega_{\text{SO}}(w_y \rightarrow \infty)$ as a function of the channel width, w_y , as determined from Monte-Carlo simulations of the acoustic spin transport under SO fields with BIA and SIA symmetries. The simulations were carried out assuming a mobility $\mu = 4m^2/(Vs)$ and temperature $T = 10$ K.

Dimensionality effects on the spin dynamics

One interesting observation in connection with Figs. 4 and 5(b) is that the spin transport lengths in the QWRs are much shorter than the ones in the DQDs, despite the much smaller lateral confinement dimensions in the former structures. To understand the impact of the lateral confinement and motional narrowing effects on the spin dynamics, we have carried out Monte-Carlo simulations of the acoustic spin transport for channels with different widths w_y . The results are summarized in Fig. 6. As expected from motional narrowing in the regime of 1D spin transport ($w_y < L_{\text{SO}}^{(2\text{D})}$), ℓ_s increases with decreasing channel width as $\ell_s \propto w^{-n_w}$ with $n_w = 2$ [13]. In addition, we observe similar dependencies of ℓ_s on the channel width for BIA and SIA SO fields.

By using $L_{\text{SO}}^{(2\text{D})} = \ell_s \sim 12 \mu\text{m}$ (as for the QW in Fig. 4), the enclosure of electrons in DQDs defined by $\lambda_{\text{SAW}} = 5.6 \mu\text{m}$ should increase ℓ_s by a factor of $(2L_{\text{SO}}^{(2\text{D})}/\lambda_{\text{SAW}})^2 \sim 18$. Such a mechanism qualitatively explains the long spin transport lengths by DQDs. It also predicts huge spin lifetimes and transport lengths for the QWRs, which are, however, not observed in the experiments. A possible explanation lies on the nature of the lateral confinement potential: while purely electrostatic for DQDs, it is imposed by structural interfaces in the QWRs. Spin dephasing due to frequent scattering events at these interfaces (known as Elliot-Yafet processes[39]), as previously postulated for QWRs,[14, 40] as well as interface-related SO fields may thus limit ℓ_s in structural channels.

A further remarkable experimental result is the weak SAW amplitude dependence of the spin precession rate Ω_{SO} for transport in QW structures as compared to QWRs and DQDs [cf. Figs. 4(a) and 5(a)]. This behaviour in QWs also contrasts with the TB predictions as well as with the model leading to Eq. (2). Furthermore, it is at odds with the Monte-Carlo simulations illustrated in Fig. 6(b), which yield the dependence of the spin precession length on channel width. Here, $r_{\Omega_{\text{SO}}} = \Omega_{\text{SO}}(w_y)/\Omega_{\text{SO}}(w_y \rightarrow \infty)$ is the ratio between the precession frequencies in a channel with finite width w_y to the one in an unconstrained channel. One finds that $r_{\Omega_{\text{SO}}}$ is essentially independent of the channel width. This result, which applies for SO fields of both BIA and SIA symmetries, can be qualitatively understood by taking into account that the spin precession rate $\Omega_{\text{SO}}(w_y)$ along the SAW propagation direction (x) is determined by the carrier velocity component along x , which remains equal to the SAW velocity as the carriers diffuse in the lateral direction [41].

We now briefly address a mechanism that can account for the weak dependence of Ω_{SO} on SAW amplitude observed for the QW. This mechanism is based on fluctuations in the storage phase ϕ_{SAW} of the carriers in the SAW potential during the transport. The driving force for this transport is the longitudinal component of the SAW piezoelectric field given by $F_x = -e\partial\Phi_{\text{SAW}}/\partial x$. In the previous sections, we have assumed that the electron spins remain at the SAW phase $\tilde{\phi}_{\text{SAW}} = 0$ corresponding to the minimum of the piezoelectric energy $-e\Phi_{\text{SAW}}$, as illustrated in Fig. 5(a). At these phases, however, F_x vanishes. To sustain a steady-state motion at the SAW velocity, both electrons (superscript e) and holes (h) must concentrate around a phase $\tilde{\phi}_{\text{SAW}}^{(i)}$ ($i = e, h$) of the SAW potential satisfying $\sin(\tilde{\phi}_{\text{SAW}}^{(i)}) = r_d^{(i)} = v_{\text{SAW}}/(\mu^{(i)}F_z)$ [rather than at $\phi_{\text{SAW}} = 0$, cf. Fig. 5(a)]. At these phases, the SAW-induced SO fields are reduced by a factor $\cos(\tilde{\phi}_{\text{SAW}}^{(i)}) = (1 - (r_d^{(i)})^2)^{1/2}$ with respect to their maximum at $\phi_{\text{SAW}} = 0$. As a result, the effective spin precession frequency reduces and becomes dependent on the effective carrier mobility. Due to the narrower thickness w_z , the transport mobility $\mu^{(i)}$ in the QWs is expected to be lower than in the QWR and DQD cases (the ambipolar mobility scales with w_z^{-6} in undoped QWs [42]), thus reducing the SAW-induced SO fields relative to the Dresselhaus contribution. As mentioned in connection with Fig. 4(a), ℓ_s increases with SAW power for the spins in the QW, thus indirectly indicating a connection between the mobility and the spin dynamics. According to this mechanism, the lower efficiency of the spin gates in the QW arises from the lower ambipolar mobility relative to the QWR and the DQDs due to its smaller thickness. Further studies are, however, required to quantify the impact of this effect.

III. DISCUSSION

In this work, we have demonstrated the ability to acoustically transport and, simultaneously, control the polarization of electrons spins stored within moving potential dots defined by SAWs in GaAs QWs and QWRs. Within the flying control gates, the spins precess around a SAW-induced SO field, and the precession rate can be dynamically changed by a factor of over 2.5 by varying the SAW amplitude, which enabled the controlled flip of the spin polarization. The experimental results for the precession rates markedly exceed previous results and agree well with the predictions of an analytical model for the SAW-induced spin-orbit fields as well as with microscopic tight-binding calculations. The latter of which enable a precise determination of the strain related spin-orbit parameters. We have also addressed the mechanisms governing spin relaxation while considering the role of the carrier mobility and of the lateral interfaces on the spin dynamics. Here, the shorter spin transport lengths measured in structurally defined QWRs as compared to electrostatically defined DQDs are attributed to spin dephasing via frequent scattering at the lateral (Al,Ga)As interfaces. Details of the scattering mechanisms are, however, presently unknown and calls for additional structural studies of the QWR interfaces.

The high degree of dynamical spin control in QWRs and DQDs demonstrated here enables dynamic control by simply chang-

ing the acoustic amplitude of the carrier wave. An obvious and important advantage is that both spin transport and manipulation can be performed through this flying spin gate in a single structure (e.g., a QWR) without requiring extra components (e.g., electrostatic gates for Rashba spin control). The experiments in Fig. 3(b) directly illustrate an electro-optical polarization modulators based on this approach. Here, the circular polarization of the PL can be set to an arbitrary value by simply varying the SAW amplitude. This functionality can be naturally extended to the transport of single spins[22] as well as for the generation of polarized single photons[15], thus enabling the realization of a spin-based quantum information processor with a photonic interface.

IV. METHODS

QWR Sample Fabrication

The planar QWRs used in this work were fabricated using MBE by overgrowing a 10 nm-thick QW on a GaAs(001) substrate pre-patterned with shallow (approximately 30 nm high) rectangular ridges [cf. Fig. 2(a)] [30]. The anisotropic nature of the MBE growth induces a local thickening of the QW at the ridge sidewalls oriented along the $\tilde{x}||[110]$ -direction along the surface, thus forming a QWR parallel to this sidewall. The thickness and width of the QWR are (25 ± 5) nm and (200 ± 5) nm, respectively, as determined by scanning transmission electron microscopy [30]. The moving potential dots for carrier and spin transport are created by propagating a SAW with a wavelength $\lambda_{\text{SAW}} = 4 \mu\text{m}$ (frequency of 726 MHz at 15 K and velocity $v_{\text{SAW}} = 2904$ m/s) along the wire axis. The SAW is generated by a split-finger interdigital transducer deposited on the sample surface. Its amplitude will be quantified in terms of the linear acoustic power density P_{SAW} , defined as the ratio between the coupled acoustic power and the width of the SAW beam. During the acoustic transport, the carriers are confined within dots with dimensions equal to the QWR width and less than $\sim \lambda_{\text{SAW}}/2$ along the directions perpendicular and parallel to the SAW propagation, respectively. Acoustic spin transport was also investigated in the QW embedding the QWR. In this case, carrier motion is unconstrained in the direction perpendicular to the transport.

DQD Sample Fabrication

The DQDs were created via the interference of two orthogonal SAW beams propagating along the $\tilde{x}||[110]$ and $\tilde{y}||[\bar{1}10]$ directions of a 30 nm thick QW on GaAs(001) [15]. The interference of the piezoelectric fields of the SAWs creates an array of DQDs propagating along the $\tilde{x}'||[010]$ surface direction [15]. DQDs yield the longest, so far, reported acoustic spin transport distances [15, 43]. SAWs with a wavelength of $\lambda_{\text{SAW}} = 5.6 \mu\text{m}$ were used and yield DQDs with dimensions of approximately $\lambda_{\text{SAW}}/2 \times \lambda_{\text{SAW}}/2$ propagating with a velocity $v_{\text{DQD}} = \sqrt{2}v_{\text{SAW}} = 4115$ m/s.

Photoluminescence measurements

The spectroscopic photoluminescence (PL) studies of the spin transport were performed at low temperatures (10-20 K) in a microscopic PL setup with radio-frequency (rf) wiring for SAW excitation. The spins were optically excited using a circularly polarized laser beam with tunable wavelength (λ_L between 760 and 808 nm) focused onto a $\sim 2 \mu\text{m}$ wide spot on the sample surface. The PL emitted along the SAW path with left- (I_L) and right-hand (I_R) circular polarization was collected with spatial resolution and used to determine the spin polarization [44] $\rho_s = (I_R - I_L)/(I_R + I_L)$ [45]. Since hole-spin relaxation in QWs and QWRs is typically much faster than the one for electrons [46], ρ_s essentially reflects the electron spin dynamics.

Tight-binding Calculations

The analytical model for the SO fields applies for a QW with infinite potential barriers and, thus, neglects the effects of the QW interfaces. In addition, the model neglects the impact of the SAW field on the electronic states, which can be significant for the valence band states in wide QWs [47]. The the SO field Ω_{SO} contributions were calculated in QWs using the tight-binding (TB) method [37, 38]. The effects of the SAW were taken into account by using the strain and piezoelectric fields to determine the atomic positions and on-site potentials, respectively, within the TB supercell [48].

Monte Carlo spin dynamics

In the calculations, the spins are assumed to move along the x -direction with the SAW velocity while having a random motion along the y -direction with mean-free-path ℓ_p and thermal velocity v_p defined by the electron mobility μ and temperature [49]. Figure 6(a) and (b) display the simulated dependence of ℓ_s and Ω_{SO} for transport in channels with different widths w_y under BIA and SIA SO fields. The SO fields were assumed to have an amplitude $\Omega_{SO}^{(2D)} = 2\pi v_{SAW}/L_{SO}^{(2D)}$ dictated by a spin precession period $L_{SO}^{(2D)} = 12 \mu\text{m}$ similar to the ones measured for QWs in Fig. 3. We further assumed $\mu = 4m^2/(Vs)$ and $T = 4 \text{ K}$, which yield $\ell_p = 0.1 \mu\text{m}$.

V. AUTHOR CONTRIBUTIONS

P.L.J.H. performed the experiments and analysis on the QW and QWR samples, and J.A.H.S. performed the experiments and analysis using the DQDs. K.B. performed the MBE growth of the samples. Initial discussions and experimental design and development between H.S., Y.K., and P.L.J.H. were critical inputs to the presented results. P.V.S. led the theory calculations and supervised the project. P.L.J.H., P.V.S., and J.A.H.S. wrote the manuscript with input from the other authors.

ACKNOWLEDGMENTS

We thank S. Ludwig for discussions and for a critical reading of the manuscript, A.C. Poveda for the help with the graphics, as well as S. Rauwerdink for the help in the fabrication of the samples. J. Stotz would also like to acknowledge the Natural Science and Engineering Research Council of Canada and the Alexander von Humboldt Foundation. This project has received funding from the European Union's Horizon 2020 research and innovation program under grant agreement No 642688.

-
- [1] S. Datta and B. Das, Electronic analog of the electro-optic modulator, *Appl. Phys. Lett.* **56**, 665 (1990).
 - [2] Y. A. Bychkov and E. I. Rashba, Oscillatory effects and the magnetic susceptibility of carriers in inversion layers, *J. Phys. C* **17**, 6039 (1984).
 - [3] H. C. Koo, J. H. Kwon, J. Eom, J. Chang, S. H. Han, and M. Johnson, Control of spin precession in a spin-injected field effect transistor, *Science* **325**, 1515 (2009).
 - [4] P. Chuang, S.-C. Ho, L. W. Smith, F. Sfigakis, M. Pepper, C.-H. Chen, J.-C. Fan, J. P. Griffiths, I. Farrer, H. E. Beere, G. A. C. Jones, D. A. Ritchie, and T.-M. Chen, All-electric all-semiconductor spin field-effect transistors, *Nat. Nanotechnol.* **10**, 35 (2015).
 - [5] M. I. D'yakonov and V. I. Perel', Spin orientation of electrons associated with the interband absorption of light in semiconductors, *SPJETP* **33**, 1053 (1971).
 - [6] Y. Ohno, R. Terauchi, T. Adachi, F. Matsukura, and H. Ohno, Spin relaxation in GaAs(110) quantum wells, *Phys. Rev. Lett.* **83**, 4196 (1999).
 - [7] A. Hernández-Mínguez, K. Biermann, R. Hey, and P. V. Santos, Electrical suppression of spin relaxation in GaAs(111)B quantum wells, *Phys. Rev. Lett.* **109**, 266602 (2012).
 - [8] B. A. Bernevig, J. Orenstein, and S.-C. Zhang, Exact SU(2) symmetry and persistent spin helix in a spin-orbit coupled system, *Phys. Rev. Lett.* **97**, 236601 (2006).
 - [9] J. D. Koralek, C. P. Weber, J. Orenstein, B. A. Bernevig, S.-C. Zhang, S. Mack, and D. D. Awschalom, Emergence of the persistent spin helix in semiconductor quantum wells, *Nature* **458**, 610 (2009).
 - [10] M. P. Walser, C. Reichl, W. Wegscheider, and G. Salis, Direct mapping of the formation of a persistent spin helix, *Nat. Phys.* **8**, 757 (2012).
 - [11] A. Balocchi, Q. H. Duong, P. Renucci, B. L. Liu, C. Fontaine, T. Amand, D. Lagarde, and X. Marie, Full electrical control of the electron spin relaxation in GaAs quantum wells, *Phys. Rev. Lett.* **107**, 136604 (2011).
 - [12] J. M. Kikkawa and D. D. Awschalom, Lateral drag of spin coherence in gallium arsenide, *Nature* **397**, 139 (1999).
 - [13] A. A. Kiselev and K. W. Kim, Progressive suppression of spin relaxation in two-dimensional channels of finite width, *Phys. Rev. B* **61**, 13115 (2000).
 - [14] A. W. Holleitner, V. Sih, R. C. Myers, A. C. Gossard, and D. D. Awschalom, Suppression of spin relaxation in submicron InGaAs wires, *Phys. Rev. Lett.* **97**, 036805 (2006).
 - [15] J. A. H. Stotz, R. Hey, P. V. Santos, and K. H. Ploog, Coherent spin transport via dynamic quantum dots, *Nat. Mater.* **4**, 585 (2005).
 - [16] H. Sanada, Y. Kunihashi, H. Gotoh, K. Onomitsu, M. Kohda, J. Nitta, P. V. Santos, and T. Sogawa, Manipulation of mobile spin coherence using magnetic-field-free electron spin resonance, *Nat. Phys.* **9**, 280 (2013).
 - [17] C. Rocke, A. O. Govorov, A. Wixforth, G. Böhm, and G. Weimann, Exciton ionization in a quantum well studied by surface acoustic waves, *Phys. Rev. B* **57**, R6850 (1998).
 - [18] M. Z. Maialle, E. A. de Andrada e Silva, and L. J. Sham, Exciton spin dynamics in quantum wells, *Phys. Rev. B* **47**, 15776 (1993).

- [19] T. Sogawa, P. V. Santos, S. K. Zhang, S. Eshlaghi, A. D. Wieck, and K. H. Ploog, Transport and lifetime enhancement of photoexcited spins in GaAs by surface acoustic waves, *Phys. Rev. Lett.* **87**, 276601 (2001).
- [20] A. Hernández-Mínguez, K. Biermann, R. Hey, and P. V. Santos, Spin transport and spin manipulation in (110) and (111) GaAs quantum wells, *Phys. Status Solidi B* **251**, 1736 (2014).
- [21] H. Sanada, T. Sogawa, H. Gotoh, K. Onomitsu, M. Kohda, J. Nitta, and P. V. Santos, Acoustically induced spin-orbit interactions revealed by two-dimensional imaging of spin transport in GaAs, *Phys. Rev. Lett.* **106**, 216602 (2011).
- [22] B. Bertrand, S. Hermelin, S. Takada, M. Yamamoto, S. Tarucha, A. Ludwig, A. D. Wieck, C. Bäuerle, and T. Meunier, Fast spin information transfer between distant quantum dots using individual electrons, *Nat. Nanotechnol.* **11**, 672 (2016).
- [23] M. I. D'yakonov, I. A. Merkulov, and V. I. Perel', Optical-orientation anisotropy produced in semiconductors by quadrupole splitting of the spin levels of the lattice nuclei, *SPJETP* **49**, 160 (1979).
- [24] G. E. Pikus, V. A. Marushchak, and A. N. Titkov, Spin splitting of energy bands and spin relaxation of carriers in cubic III-V crystals (review), *Sov. Phys. Semicond.* **22**, 115 (1988).
- [25] Y. Kato, R. C. Myers, A. C. Gossard, and D. D. Awschalom, Coherent spin manipulation without magnetic fields in strained semiconductors, *Nature* **427**, 50 (2004).
- [26] M. Beck, C. Metzner, S. Malzer, and G. H. Doehler, Spin lifetimes and strain-controlled spin precession of drifting electrons in zinc blende type semiconductors, *Europhys. Lett.* **75**, 597 (2006).
- [27] D. J. English, P. G. Lagoudakis, R. T. Harley, P. S. Eldridge, J. Hübner, and M. Oestreich, Strain-induced spin relaxation anisotropy in symmetric (001)-oriented GaAs quantum wells, *Phys. Rev. B* **84**, 155323 (2011).
- [28] K. Biermann, O. D. D. Couto, Jr., E. Cerda, H. B. de Carvalho, R. Hey, and P. V. Santos, Spin transport in (110) GaAs-based cavity structures, *J. Supercond. Novel Magn.* **23**, 27 (2010).
- [29] J. A. H. Stotz, R. Hey, P. V. Santos, and K. H. Ploog, Spin transport and manipulation by mobile potential dots in GaAs quantum wells, *Physica E* **32**, 446 (2006).
- [30] P. L. J. Helgers, H. Sanada, Y. Kunihashi, A. Rubino, C. Christopher J. B. Ford, K. Biermann, and P. V. Santos, Sidewall quantum wires on GaAs (001) substrates, *Phys. Rev. Applied* **11**, 064017 (2019).
- [31] S. Lazić, R. Hey, and P. Santos, Mechanisms for non-classical light emission from acoustically populated (311)A GaAs quantum wires, *New J. of Phys.* **14**, 013005 (2012).
- [32] See Supplemental Material, Sec. SM2 at URL for details about the determination of the spin transport length.
- [33] M. M. de Lima, Jr. and P. V. Santos, Modulation of photonic structures by surface acoustic waves, *Rep. Prog. Phys.* **68**, 1639 (2005).
- [34] See Supplemental Material, Sec. SM5 at URL for details about the contributions of the SAW strain fields to the spin-orbit interaction.
- [35] See Supplemental Material, Sec. SM3 at URL for details about the contributions of the SAW strain fields to the spin-orbit interaction.
- [36] G. Dresselhaus, Spin-orbit coupling effects in zinc blende structures, *Phys. Rev.* **100**, 580 (1955).
- [37] P. V. Santos and M. Cardona, Comment on: Observation of spin precession in GaAs inversion layers using antilocalization, *Phys. Rev. Lett.* **72**, 432 (1994).
- [38] P. V. Santos, M. Willatzen, M. Cardona, and A. Cantarero, Tight-binding calculations of spin splittings in semiconductor superlattices, *Phys. Rev. B* **51**, 5121 (1995).
- [39] R. J. Elliott, Theory of the effect of spin-orbit coupling on magnetic resonance in some semiconductors, *Phys. Rev.* **96**, 266 (1954).
- [40] F. Alsina, J. A. H. Stotz, R. Hey, U. Jahn, and P. V. Santos, Acoustic charge and spin transport in GaAs quantum wires, *Phys. Status Solidi C* **9**, 2907 (2008).
- [41] See Supplemental Material, Sec. SM6 at URL for details about the dependence of the precession rate determined by the Monte-Carlo simulations on the channel width.
- [42] Z. Vörös, R. Balili, D. W. Snoke, L. Pfeiffer, and K. West, Long-distance diffusion of excitons in double quantum well structures, *Phys. Rev. Lett.* **94**, 226401 (2005).
- [43] J. A. H. Stotz, P. V. Santos, R. Hey, and K. H. Ploog, Mesoscopic spin confinement during acoustically induced transport, *New J. Phys.* **10**, 093013 (2008).
- [44] M. I. Dyakonov, *Spin physics in semiconductors* (Springer, 2008).
- [45] See Supplemental Material, Sec. SM1 at URL for further details about the experimental determination of the spin polarization.
- [46] B. Baylac, X. Marie, T. Amand, M. Brousseau, J. Barrau, and Y. Shekun, Hole spin relaxation in intrinsic quantum wells, *Surf Sci* **326**, 161 (1995).
- [47] P. V. Santos, F. Alsina, J. A. H. Stotz, R. Hey, S. Eshlaghi, and A. D. Wieck, Band mixing and ambipolar transport by surface acoustic waves in GaAs quantum wells, *Phys. Rev. B* **69**, 155318 (2004).
- [48] See Supplemental Material, Sec. SM4 at URL for further details about the tight-binding calculation procedure.
- [49] See Supplemental Material, Sec. SM6 at URL for details about the Monte-Carlo simulations.

Supplementary Material: Flying electron spin control gates

Paul L. J. Helgers,^{1,2} James A. H. Stotz,^{3,4} Haruki Sanada,²
Yoji Kunihashi,² Klaus Biermann,³ and Paulo V. Santos^{3,*}

¹*Paul-Drude-Institut für Festkörperelektronik, Leibniz-Institut im
Forschungsverbund Berlin e.V., Hausvogteiplatz 5-7, 10117 Berlin, Germany*

²*NTT Basic Research Laboratories, NTT Corporation,
3-1 Morinosato-Wakamiya, Atsugi, Kanagawa 243-0198, Japan*

³*Paul-Drude-Institut für Festkörperelektronik, Leibniz-Institut im
Forschungsverbund Berlin e. V., Hausvogteiplatz 5-7, 10117 Berlin, Germany*

⁴*Department of Physics, Engineering Physics & Astronomy,
Queen's University, Kingston, ON, K7L 3N6 Canada*

(Dated: November 23, 2021)

SM1. SPIN POLARIZATION MEASUREMENTS

The spectroscopic photoluminescence (PL) studies of the spin transport were carried out in a helium flow cryostat (10-20 K) with optical access and radio-frequency wiring for SAW excitation. The spins were optically excited using a circularly polarized laser beam from a tunable Ti-sapphire laser (wavelengths λ_L between 760 and 808 nm) focused onto a $\sim 2 \mu\text{m}$ wide spot on the sample surface by a 20x objective [L in Fig. 2(c) of the main text]. The same objective collects the PL emitted from along the SAW path and directs it to a triple-grating spectrometer operating in the subtractive mode and equipped with a cooled CCD detector. Spatially resolved PL maps are recorded by imaging the acoustic transport path onto the input slit of the spectrometer. An optical arrangement consisting of a quarter wave plate and a beam polarization displacer placed in front of the spectrometer slit shifts the PL images with right (I_R) and left (I_L) hand circular polarizations along the slit direction. In this way, we simultaneously record PL images of the spatial distribution of the two polarizations on the CCD.

The spin polarization ρ_s during acoustic transport can be determined by exciting spins with a right hand circularly polarized laser beam and detecting the PL intensities I_R and I_L according to:

$$\rho_s = \frac{I_R - I_L}{I_R + I_L}. \quad (\text{SM1})$$

Since hole-spin relaxation in QWs and QWRs is typically much faster than for electrons [1], we assume that ρ_s reflects only the electron spin dynamics.

In order to correct for artifacts arising from dichroism of the optical components of the setup, the polarization experiments were carried out by recording PL maps excited with a right-hand and then a left-hand circularly polarized laser beam. We will denote the corresponding

PL intensities as I_{LL} , I_{LR} , I_{RL} and I_{RR} , where the first (second) index corresponds to the circular polarization of the excitation (PL emission). For an ideal optical system (i.e., with transmission independent of the polarization), one expects a ratio

$$a_r^2 = \frac{I_{LL}I_{RL}}{I_{RR}I_{LR}} = \frac{t_L}{t_R} \quad (\text{SM2})$$

equal to unity. The presence of dichroic elements in the optical path makes $a_r \neq 1$. The effect of these components on the spin polarization can be corrected by using the following expression to determine the spin polarization:

$$\rho_s = \frac{a_r I_{RR} - I_{RL}}{a_r I_{RR} + I_{RL}}. \quad (\text{SM3})$$

SM2. SPIN LIFETIMES

The spin lifetimes τ_s in the absence of acoustic excitation were determined by time-resolved Kerr rotation measurements carried out in the pump-probe configuration [2]. Typical temporal Kerr traces for the QW (black) and QWR (red) are shown in Fig. SM1. The measurements were performed using an excitation energy of 1.551 eV and power density of 8 W cm^{-2} . The traces can be fitted with an exponential decaying function yielding Kerr rotation decay times $\tau_K = 200 \text{ ps}$ for the QW and $\tau_K = 1 \text{ ns}$ for the QWRs.

The spin decay time was determined by combining the Kerr rotation decay times with the carrier recombination lifetimes obtained from time resolved PL measurements. This procedure yields spin lifetimes of $\tau_s = 0.5 \text{ ns}$ and $\tau_s = 2 \text{ ns}$ for the QW and QWRs, respectively. The much longer spin lifetime in the QWR as compared to the QW is attributed to (i) the lateral confinement of the QWR carriers by the surrounding QW, leading to motional narrowing and (ii) the larger thickness of the QWR. Whereas both effects suppress D'yakonov-Perel'

* santos@pdi-berlin.de

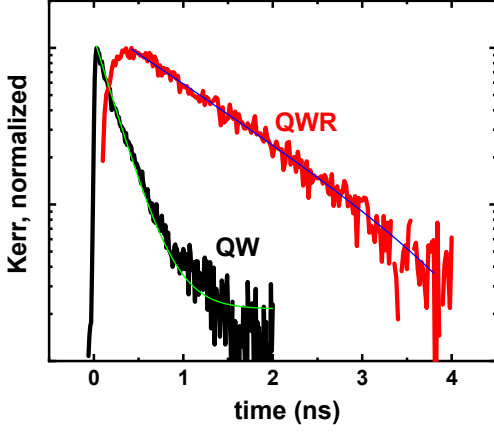


FIG. SM1. Time-resolved Kerr polarization rotation measured on the QW (black) and QWR (red). The lines are exponentially decaying functions yielding a Kerr rotation decay time of approximately 200 ps and 1 ns for the QW and the QWR, respectively.

spin relaxation [3, 4], the latter also decreases of the electron-hole exchange interaction and its associated spin relaxation ratio [5].

SM3. SAW-INDUCED SO FIELDS

In this section, we briefly summarize the SO mechanisms related to the strain and piezoelectric fields induced by a SAW. In the absence of a SAW, the conduction band spin splitting for electrons moving along the $\langle 110 \rangle$ -directions of an intrinsic GaAs QW on a (001) substrate is given by the Dresselhaus term:

$$\Omega_D \sim \pm \gamma k \left[\left(\frac{\pi}{w_z} \right)^2 - \frac{1}{2} k^2 \right], \quad (\text{SM4})$$

where γ is a material constant and $w_z = d_{QW} + 2d_0$ is the total extension of the electronic wave function, assumed to be equal to the QW width (d_{QW}) plus the penetration depth in the barrier layers (d_0). For an electron moving with the SAW velocity v_{SAW} , the wave vector k is obtained from the electron momentum according to:

$$k = \frac{m^* v_{SAW}}{\hbar}. \quad (\text{SM5})$$

where m^* is the conduction band (CB) effective mass.

A uniaxial strain leads to a linear term in the CB splitting given by:[6–8]

$$H_S = \frac{1}{2} \left[C_3 (\hat{\sigma} \vec{\phi}) + C'_3 (\hat{\sigma} \vec{\psi}) \right] \quad (\text{SM6})$$

where $\phi_z = \varepsilon'_{xz} k_z - \varepsilon'_{yz} k'_y$ and $\psi_z = k_z (\varepsilon'_{xx} - \varepsilon'_{yy})$ and cyclic permutations. The $\hat{\sigma}_i$ denote the Pauli matrices.

The apostrophe (') indicates that the strain components are relative to the conventional axes x' , y' , and z' . This Hamiltonian gives rise to a strain-induced spin precession frequencies given by [9]

$$\hbar \Omega_S = C_3 \begin{bmatrix} \varepsilon'_{yx} k_y - \varepsilon'_{zx} k_z \\ \varepsilon'_{zy} k_z - \varepsilon'_{yx} k_x \\ \varepsilon'_{xz} k_x - \varepsilon'_{yz} k_y \end{bmatrix} + C'_3 \begin{bmatrix} k_x (\varepsilon'_{yy} - \varepsilon'_{zz}) \\ k_y (\varepsilon'_{zz} - \varepsilon'_{xx}) \\ k_z (\varepsilon'_{xx} - \varepsilon'_{yy}) \end{bmatrix} \quad (\text{SM7})$$

In order to address the SAW strain field, it is convenient to use a reference frame with the x -axis along the SAW propagation direction, the y -axis on the sample surface and perpendicular to x , and the z -axis perpendicular to the surface. A SAW propagating along the $[110]$ - or $[\bar{1}10]$ -directions of the (001) surface induces three non-vanishing engineering strain components u_{xx} , u_{zz} , and u_{xz} . Furthermore, we use u_{ij} to denote the engineering strain components and, thus, to distinguish them from the physical strain ones $\varepsilon_{i,j}$ ($\varepsilon_{ij} = u_{ij}$ for $i = k$ and $\varepsilon_{ij} = u_{ij}/2$ for $i \neq j$).

In a piezoelectric material, the strain field from the SAW generates a piezoelectric polarization field D given by

$$D = e_{14} [u_{xz}, 0, u_{xx}]^T, \quad (\text{SM8})$$

where the superscript T denotes the vector transposition operation. When the SAW fields are transformed to the Cartesian reference frame, the strain and electrical polarization fields become:

$$\varepsilon' = \left[u_{xx}/2, u_{xx}/2, u_{zz}, \pm u_{xz}/\sqrt{2}, u_{xz}/\sqrt{2}, \pm u_{xx} \right]^T \quad (\text{SM9})$$

$$D' = e_{14} [2u_{xz}, 0, u_{xx}]^T, \quad (\text{SM10})$$

where upper and lower signs apply for SAWs propagating along the $[110]$ - and $[\bar{1}10]$ -directions, respectively. By substituting Eq. SM9 into Eq. SM7 one obtains:

$$\hbar \Omega_S = \frac{1}{2\sqrt{2}} k [C_3 u_{xx} + C'_3 (u_{xx} - 2u_{zz})] \begin{bmatrix} 1 \\ -1 \\ 0 \end{bmatrix} \quad (\text{SM11})$$

Note that the strain induces a SO component perpendicular to the SAW propagation direction.

A SAW in a piezoelectric material also induces a transverse piezoelectric field F_z associated with D , which gives rise to a Rashba spin-orbit contribution. As a consequence, SAWs along a $\langle 110 \rangle$ induce three contributions for the CB spin splitting, all oriented in-plane and perpendicular to the SAW propagation direction, given by:

$$\hbar \Omega_{SO} = \Omega_D + \Omega_S + \Omega_R \quad (\text{SM12})$$

$$\Omega_S = \mp k \frac{1}{2} [C_3 u_{xx} + C'_3 (u_{xx} - 2u_{zz})] \quad (\text{SM13})$$

$$\Omega_R = -2kr_{41} F_z \quad (\text{SM14})$$

TABLE SM1. Tight-binding parameters used in the calculation of spin-orbit conduction band splitting. The notation used corresponds to the one of Ref. 10. In order to account for the valence band discontinuity we subtracted 0.007 eV from the diagonal parameters (i.e., E_s , E_p , and E_{s^*}) of the $\text{Al}_{0.15}\text{Ga}_{0.85}\text{As}$ barrier layers.

Parameter	GaAs[11] (eV)	$\text{Al}_{0.15}\text{Ga}_{0.85}\text{As}$ (eV)
E_s (anion)	-8.457	-8.3172
E_p (anion)	0.9275	0.92938
E_s (cation)	-2.7788	-2.53673
E_p (cation)	3.5547	3.55250
V_{ss}	-6.4513	-6.48321
V_{xx}	1.9546	1.95121
V_{xy}	4.77	4.69110
V_{s_0p} (anion,cation)	4.48	4.57360
V_{s_1p} (cation,anion)	7.85	7.49390
E_{s^*} (anion)	8.4775	8.32833
$V_{s_0p}^*$ (anion,cation)	4.8422	4.78967
$E_{s_1}^*$ (cation)	6.6247	6.64005
$V_{s_1p}^*$ (cation,anion)	7	6.69940
$3\lambda_a$ (anion)	0.39	0.39171
$3\lambda_c$ (cation)	0.174	0.15150

The upper and lower signs apply for SAWs along the $[110]$ and $[\bar{1}10]$ directions, respectively. We will show in Sec. SM4 A that the C'_3 term in Eq. SM13 is much smaller than the one associated with C_3 . This term will be neglected in the main text and in the subsequent analyses.

SM4. TIGHT-BINDING CALCULATIONS OF SPIN SPLITTINGS IN QWS

We present in this section details about the calculations of the spin splitting of the conduction band of GaAs QWs under SAW fields. In bulk GaAs, this splitting results from a three-band coupling process involving the s-like GaAs conduction band and the p-like conduction and valence bands [12]. The three-band interaction process leads to the cubic dependence of the spin splitting on wave vector k . Calculation of the splitting requires, therefore, that one takes into account interactions between of all these bands. As demonstrated in Ref. 12, this can be carried out using ab-initio approaches or empirical approaches using a large number of bands (e.g., a 14 band $\mathbf{k} \cdot \mathbf{p}$ method). Here, we determine the splittings using the empirical tight-binding (TB) method[13] following the approach described in Refs. 14 and 15. This atomistic approach enables the determination of the band structure of QWs with widths up to a few tens of nanometres using moderate computational efforts. Although empirical in the sense that it uses parameters fitted to the bulk band structure, it can be regarded as “microscopic” when compared with other approaches such as the $\mathbf{k} \cdot \mathbf{p}$ effective mass calculations.

The TB calculations were carried out using a basis consisting of sp^3s^* orbitals [16] including spin-orbit coupling[17, 18]. This orbital basis consists of 10 or-

bitals per atom and includes only nearest-neighbour interactions. It has been shown to reproduce very well the highest valence and the lowest conduction bands of most bulk semiconductors[16]. The tight-binding parameters employed for the GaAs QW and the $\text{Al}_{0.15}\text{Ga}_{0.85}\text{As}$ barrier layers are summarized in Table SM1.

The calculations were performed for an electron with wave vector given by Eq. SM5 in a periodic supercell consisting of a single QW with sandwiched between 4.5 nm wide $\text{Al}_{0.15}\text{Ga}_{0.85}\text{As}$ barriers. The atomic positions within the unit cell were deformed in order to take into account the effects of the SAW strain field determined in the previous section. The effects of the piezoelectric field F_z were incorporated in the calculations by adding the position-dependent electrostatic energy to the on-site TB parameters. The following convention applies for the crystallographic orientation of the axes:

- in the unit cell, the anion (As) sits at the origin while the cation (Ga) is at $(a_0/4)(111)$ (this is the same as in Ref. 12);
- a positive (piezo) electric field corresponds to a field along the growth direction.

A. Tight-binding calculation of the spin-orbit strain coefficients

As discussed in Sec. SM3, the SAW strain induces SO contributions described by two material constants C_3 and C'_3 . Reported values for these contributions span a wide range: $C_3 = 0.47$ eVnm [19], $C_3 = 0.52$ eVnm [6], and $C_3 = 0.81$ eVnm [9]. C'_3 has not been measured (nor calculated), and should be negligible in comparison with C_3 . In this section, we use the TB approach to estimate the magnitude of these contributions.

We determined the strain coefficients C_3 and C'_3 by performing TB calculations for GaAs under strain and fitting to the expressions in Eq. SM12. C'_3 was calculated using a strain field with $u_{xx} = 0$, $u_{xz} = 0$, and for different values for u_{zz} . The results are summarized in Fig. SM2(b). We find that C'_3 is essentially zero.

In order to calculate C_3 , we took $u_{zz} = 0$, $u_{xz} = 0$ and performed calculations for different u_{xx} [Fig. SM2(a)]. The TB calculations yield $|C_3| = 1.65$ eVnm. This C_3 value agrees very well with the experimental one obtained from the QWR data in the main text. It is, however, twice as large as the one experimentally determined by Beck (0.81 eVnm), [9] and also larger than the one estimated from D'yakonov's calculations. [7, 20] Corresponding results for QW structures are presented in the main text.

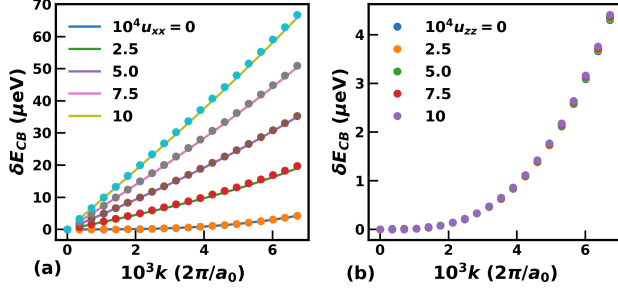


FIG. SM2. Calculations of the conduction band spin splittings in GaAs under different strain components (a) u_{xx} and (b) u_{zz} (symbols). The lines are fits to Eq. SM13 (Dresselhaus and strain parts) used to determine the coefficients $|C_3| = 1.65 \text{ eVnm}$ and $C'_3 = 0$.

SM5. EXPERIMENTAL DETERMINATION OF STRAIN-INDUCED C_3 PARAMETER

A. QWs and QWRs data

According to Eq. SM12 (and to Eq. 2 of the main text), the SO field for spins under the moving SAW field can be stated in the reference frame with axis $x = [110]$, $y = [\bar{1}10]$ and $z = [001]$ as:

$$\hbar\Omega_{SO} = \left[\gamma \left[\frac{\pi}{w_z} \right]^2 - 2F_z r_{41} - \frac{C_3 u_{xx}}{2} \right] k_x. \quad (\text{SM15})$$

Here, k_x is given by Eq. SM5 and $w_z = d_{QW} + 2d_B$ is the extension of the electron wave function along the z -direction given by the sum of the nominal QW width (d_{QW}) and the penetration depths in the upper and lower QW barriers (d_B). In the calculations that follow, we assume $d_B = 2 \text{ nm}$. The spin-orbit parameters are given by $\gamma = 17 \times 10^{-30} \text{ eV m}^3$ (Dresselhaus [21]), $r_{41} = -5.95 \times 10^{-20} \text{ e m}^2$ (Bychkov-Rashba [4]) and C_3 the strain parameter.

As mentioned in the main text, F_z is proportional to u_{xx} . In order to determine the proportionality constant, we conducted numerical simulations of the acoustic and piezoelectric fields of a SAW with a wavelength $\lambda_{SAW} = 4 \mu\text{m}$ propagating along the $[110]$ -direction (see Ref. 22 for details). Figure SM3(a) shows the relative values of the SAW potential Φ_{SAW} (black), u_{xx} (blue), and F_z (red) at various positions/phases of the wave. The curves are normalized to their maximum values and shifted along the vertical axis for clarity. For this propagation direction, the maxima of Φ_{SAW} , corresponding to the transport phase of electrons (brown circles with minus sign), F_z is negative (i.e., oriented along the $-z$ direction). The uniaxial strain u_{xx} is positive at this position. Thus, $u_{xx} > 0$ and $F_z < 0$ in Eq. (SM15).

Figure SM3(b) shows the amplitude of the piezoelectric field $|F_z|$ as a function of the strain u_{xx} . The up-

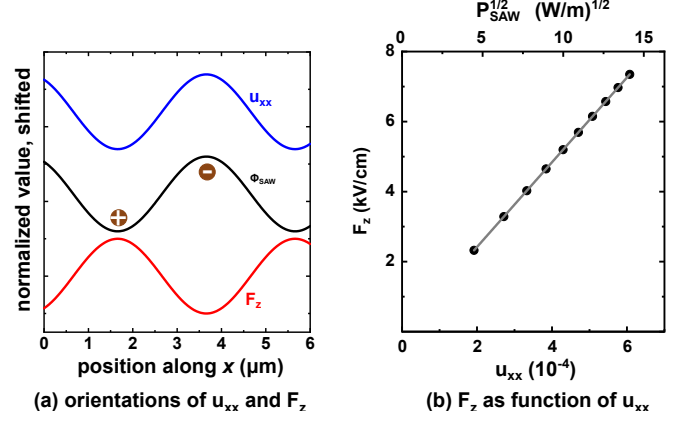


FIG. SM3. (a) Relative orientations of Φ_{SAW} (black), F_z (red) and u_{xx} (blue) along the QWR axis. The transport position of electrons (holes) in the case of ideal acoustic transport is depicted by brown circles with a minus (plus) sign. (b) Dependence of $|F_z|$ on u_{xx} . The upper horizontal scale displays the square root $\sqrt{P_\ell} \propto u_{xx,0}$, thus establishing the relationship between the strain amplitude and the linear acoustic power density generated by the IDT.

per horizontal scale displays the corresponding values for $\sqrt{P_\ell} \propto u_{xx}$, thus establishing the relationship between the strain amplitude and the linear acoustic power density P_ℓ excited by the IDT. The linear fit yields a slope of $r_{SF} = 12 \times 10^3 \text{ kV cm}^{-1}$. Note that the strain is small, so that the resulting field is on the order of kV cm^{-1} . Substitution of the simulation results modifies Eq. (SM15) in:

$$\hbar\Omega_{SO} = \left[\gamma \left[\frac{\pi}{w_z} \right]^2 + 2r_{SF} u_{xx} r_{41} - \frac{C_3 u_{xx}}{2} \right] k_x. \quad (\text{SM16})$$

Note that the second term on the right-hand-side (corresponding to Bychkov-Rashba) turns positive due to the negative F_z .

The fits of the experimental data for QWRs in Fig. 4(b) of the main text to Eq. (SM3) were carried out using an effective electron mass $m_e^* = 0.067$ and a SAW velocity $v_{SAW} = 2904 \text{ m s}^{-1}$ yielding $C_3 = -2.6 \text{ eV nm}$. Table SM2 summarizes the calculated values for the different components of the SO field for two different SAW powers. All SO contributions are directed along the same direction (the $+y$ -axis). In addition, the strain-related SO contribution is much larger than the one from the piezoelectric field.

B. Calculation of C_3 parameter for DQDs

Due to the different orientations of the Dresselhaus and the SAW-related SO fields expressed in Eq. 3 of the main text, the amplitude of the precession frequency experienced by spins in DQDs created by the superposition

QW/QWR	Ω_D (GHz)	Ω_R (GHz)	Ω_S (GHz)	Ω_{exp} (GHz)	Ω_{calc} (GHz)
QWR, $P_{SAW} = 7$ dBm	0.51	0.03	0.20	0.89	0.74
QWR, $P_{SAW} = 21$ dBm	0.51	0.14	1.03	1.77	1.68
QW, $P_{SAW} = 7$ dBm	2.20	0.03	0.20	1.66	2.43
QW, $P_{SAW} = 21$ dBm	2.20	0.14	1.03	1.71	3.38

TABLE SM2. Spin-orbit precession frequencies in QWs and QWRs for different SAW powers.

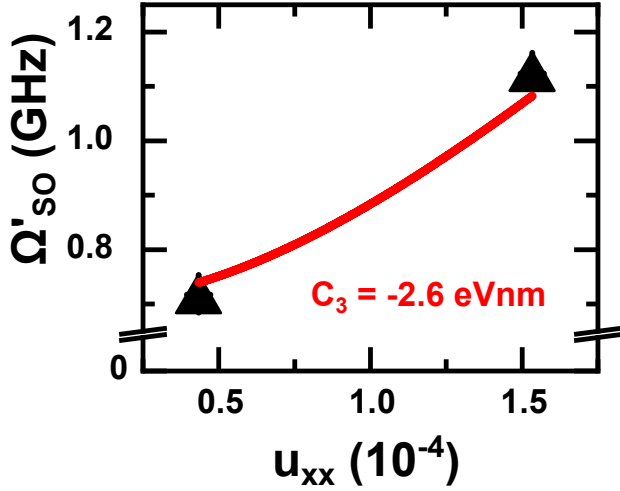


FIG. SM4. Fit of the DQD data to determine the C_3 parameter.

of SAW beams with the same intensity propagating along the x - and y -directions becomes:

$$|\Omega'_{SO}| = \sqrt{2\Omega_D^2 + 4[\Omega_R + \Omega_S]^2}, \quad (\text{SM17})$$

where, as mentioned in the main paper, Ω_D , Ω_R , and Ω_S are the magnitudes of the precession frequency for a single SAW beam along the x -direction. As in the previous case, the amplitude of the transverse piezoelectric field can be related to the strain amplitude u_{xx} by a factor $r_{SF} = 21 \times 10^3$ kV/cm. Due to the quadratic dependence of Ω'_{SO} on Ω_D in Eq. (SM17), it is not possible to determine from the DQD data in Fig. 4(b) of the main paper the relative signs of the Dresselhaus and SAW-related SO fields. The red line in Fig. SM4 shows, however, that the SAW power dependence of Ω'_{SO} is reasonably well accounted for using a value of $C_3 = -2.6$ eV nm that is comparable to the QWR results. Table SM3 summarizes the values of the different SO-precession frequencies for DQDs.

DQDs	Ω'_D (GHz)	Ω'_R (GHz)	Ω'_S (GHz)	Ω'_{exp} (GHz)	Ω'_{calc} (GHz)
$P_{SAW} = 2$ W/m ($C_3 = -2.0$)	0.53	-0.05	-0.23	0.71	0.60
$P_{SAW} = 25$ W/m ($C_3 = -2.0$)	0.53	-0.20	-0.79	1.11	1.12

TABLE SM3. Spin-orbit precession frequencies determined for transport by DQDs under different SAW powers.

SM6. MONTE-CARLO SIMULATIONS OF THE ACOUSTIC SPIN TRANSPORT

We study, in this section, the spin dynamics during acoustic transport in narrow channels using Monte-Carlo simulations of the spin trajectories. Similar Monte-Carlo investigations of the confinement effects on the spin dynamics were carried out for diffusing spins by Kiselev and Kim [3, 23]. In contrast to the results presented here, those previous studies were restricted to the transport dynamics for short spin coherence times, where spatial precession oscillations are not observed. In addition, these studies did not address the impact of carrier drift under an external field on the spin dynamics.

The Monte-Carlo simulations were performed by assuming that z ||[001]-oriented electron spins are optically excited at the position $(x, y) = (0, 0)$ at the center of a channel with width w_y . A surface acoustic wave (SAW) propagating with phase velocity v_{SAW} along x ||[110] collects the spins and transports them along the x -direction with the SAW velocity. During transport, the electron spins precess around the SO-field with angular precession frequency Ω_{SO} given by:

$$\Omega_{SO} = (1 - |r_s|)\Omega_{BIA} + r_s\Omega_{SIA}, \quad (\text{SM18})$$

where Ω_{BIA} and Ω_{SIA} are the components of the SO-field due to the bulk (BIA) and structural (SIA) inversion asymmetry, respectively, and r_s is a factor weighting the amplitude of the two components (see further details below). For small magnitudes of the electron momentum $\hbar\mathbf{k}$, these components can be expressed in the $\mathbf{k} = (k_x, k_y) = k(\cos\theta, \sin\theta)$ basis, where θ is the propagation angle with respect to the x axis, as:

$$\Omega_{BIA} = \underbrace{c_{BIA}k}_{\Omega_{BIA}^{(max)}} \begin{bmatrix} +\sin(\theta) \\ +\cos(\theta) \end{bmatrix} \quad (\text{SM19})$$

$$\Omega_{SIA} = \underbrace{c_{SIA}k}_{\Omega_{SIA}^{(max)}} \begin{bmatrix} -\sin(\theta) \\ +\cos(\theta) \end{bmatrix} \quad (\text{SM20})$$

Here, c_i ($i = \text{BIA, SIA}$) are material constants associated with the BIA and SIA components determining the precession frequencies $\Omega_i^{(max)} = c_i k$ (i.e., only linear terms in k are taken into account).

Due to the dependence on carrier momentum, the determination of the spin dynamics under the SO fields requires the knowledge of the electron trajectory during the motion. The latter was determined based on the following assumptions:

- the spins are free to diffuse along y ([110] (i.e., along the SAW wave fronts) with a velocity v_y (and corresponding momentum $m_e^* v_y$) determined from a thermal distribution given by:

$$f(v_y)\delta v_y = \left[\frac{m_e^*}{2\pi k_B T} \right]^{1/2} e^{-\frac{m_e^* v_y^2}{2k_B T}} = \frac{1}{\sqrt{\pi} v_p} e^{-v^2/v_p^2} \delta v_y, \quad (\text{SM21})$$

where $v_p = \sqrt{\frac{2k_B T}{m_e^*}}$ and T is the temperature. The diffusion along y proceeds until the spins are back-reflected at the edges of the channel.

- within the channel boundaries, the electron spins precess around the spin orbit field with an angular precession frequency Ω_{SO} [cf. Eq. (SM18)] determined by the momentum $\hbar \mathbf{k}$ until they are scattered with a scattering time τ . The scattering time τ is determined from the mobility μ according to: $\tau = m_e^* \mu / q_e$, where q_e is the electron charge. The motion along y is randomized at each scattering event.
- Due to the linear dependence of the precession frequencies on \mathbf{k} , the spin precession angle for propagation along a fixed direction only depends on the distance between the initial and final points of the trajectory. If $(\cos \theta, \sin \theta) \Delta \ell$ is the displacement vector between two successive scattering events, then the corresponding spin precession angle under a SO field Ω_{SIA} will be $\delta \phi_s = 2\pi \Delta \ell / L_{\text{SO}}^{\text{SIA}}$. Here, $L_{\text{SO}}^{\text{SIA}} = m_e^* c^{\text{SIA}} / \hbar$ is the SO length, which only depends on material properties. These results apply for $\Delta \ell \ll L_{\text{LO}}^{\text{SIA}}$ and are also valid for the BIA component. The spin dynamics results to be shown below were calculated assuming $L_{\text{SO}}^{\text{SIA}} = L_{\text{LO}}^{\text{BIA}} = L_{\text{SO}}^{(2D)} = 12 \mu\text{m}$.

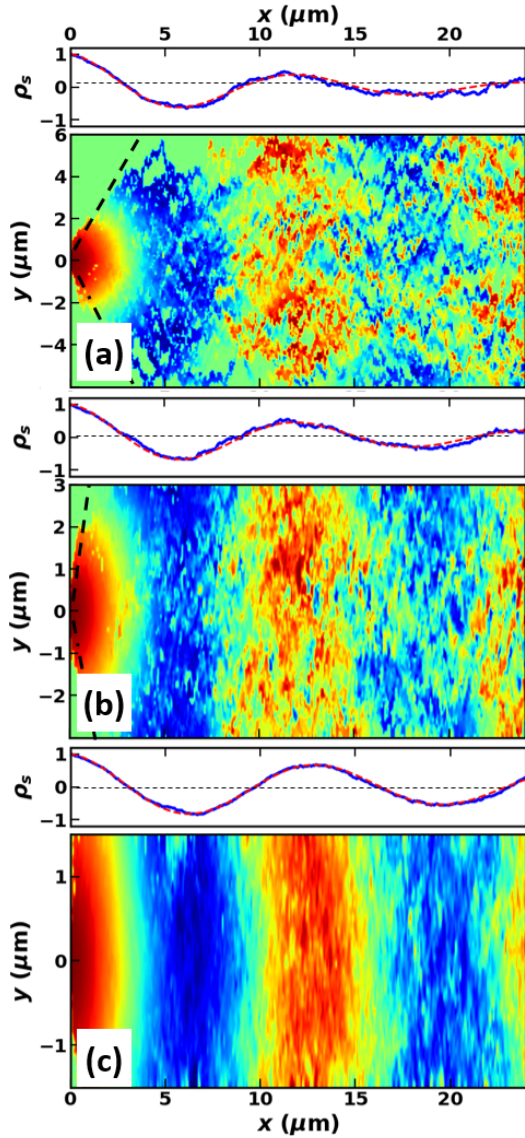


FIG. SM5. Spin polarization profiles during acoustic transport in channels with width (a) $w_y = L_{\text{SO}}^{(2D)} = 12 \mu\text{m}$, (b) $w_y = 6 \mu\text{m}$, and (c) $w_y = 3 \mu\text{m}$. The profiles result from Monte-Carlo simulations of the spin transport under a spin-orbit field with SIA asymmetry quantified by an effective spin-orbit length $L_{\text{SO}} = 12 \mu\text{m}$. The simulations assume a temperature of 10 K and carrier mobility of $4 \text{ m}^2/(\text{Vs})$. The colors encode the spin projection along z . The upper plots display the spin polarization ρ_s obtained by integrating the color maps within the range $|y| < 2 \mu\text{m}$.

- the propagation velocity v_{SAW} along x imparts a momentum along this direction given by $\hbar k_x = m_e^* v_{\text{SAW}}$, where m_e^* is the electron effective mass;

Figures SM5(a)-(c) compare spin polarization maps calculated for acoustic transport under a SO field with SIA symmetry (Ω_{SIA}) along channels with different widths w_y . In each map, the colors encode the z projection of the spin vector calculated by averaging over 40 Monte-Carlo realizations. In the wide channels [Figs. SM5(a)], the individual spin trajectories can still be identified. Here, one sees that the spins initially propagate radially from the excitation spot $(x, y) = (0, 0)$ within a cone (dashed lines) defined by the ratio between the average thermal velocity and the SAW velocity. The spin polarization within this cone oscillates along the radial direction with a precession period given by L_{SO} . For longer transport distance along x , an increasing number of trajectories with different spin polarization superimpose, leading to a decay of the average spin polarization.

The panels on top of the maps in Fig. SM5 display the average spin polarization ρ_s obtained by integrating the spin projection maps for $|y| < 2 \mu\text{m}$. The superimposed dashed lines are fits to Eq. (1) of the main text, which

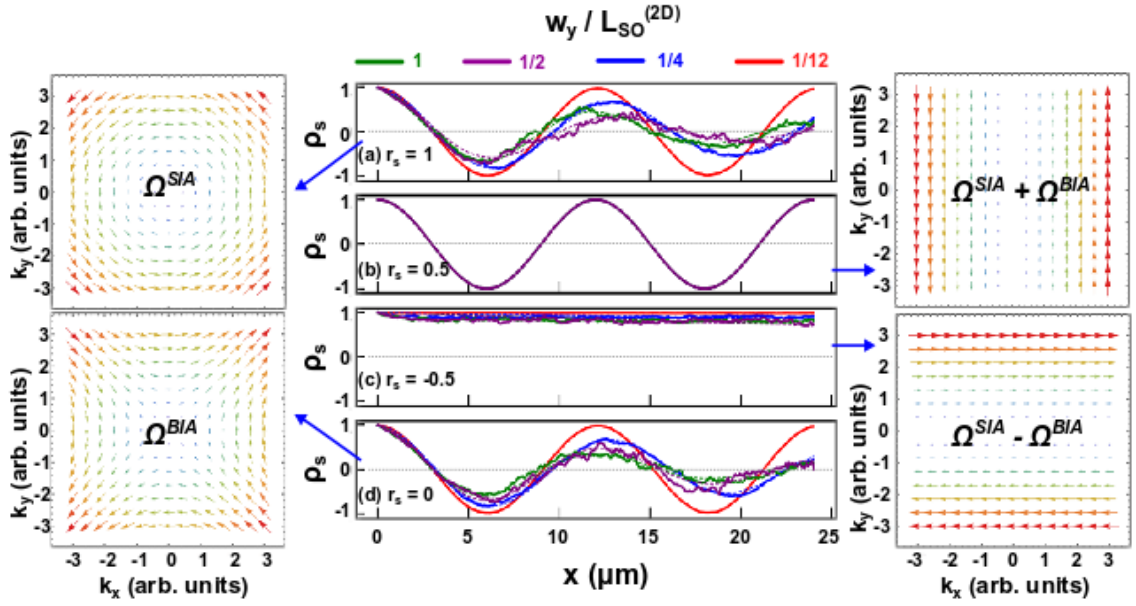


FIG. SM6. Spin polarization profiles along the SAW transport path calculated for different ratios w_y/L_{SO} and (a) $r_s = 1$ [$\Omega_{SO} = \Omega_{SIA}$, cf. Eq. (SM20)] (b) $r_s = 0.5$ ($\Omega_{SO} = (\Omega_{SIA} + \Omega_{BIA})/2$), (c) $r_s = -0.5$ ($\Omega_{SO} = (\Omega_{SIA} - \Omega_{BIA})/2$), and (d) $r_s = 0$ [$\Omega_{SO} = \Omega_{BIA}$, cf. Eq. (SM19)]. (b) and (c) are the spin helix modes with Ω_{SO} oriented along the y - and x -directions, respectively. The right and left inset display the corresponding momentum dependence of the spin-orbit field for these four configurations.

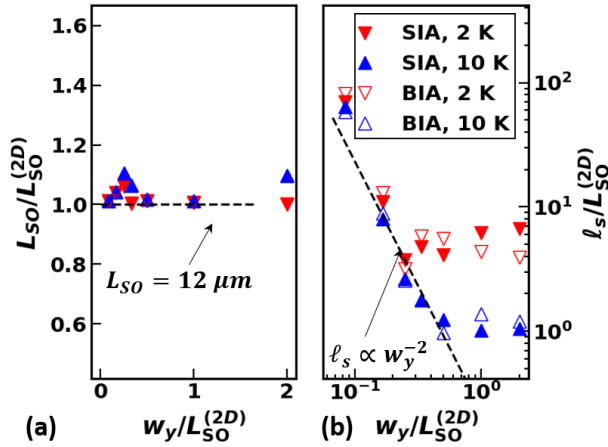


FIG. SM7. Dependence of the fitted (a) spin-orbit precession ratio $L_{SO}/L_{SO}^{(2D)}$ and (b) spin dephasing length (ℓ_s) normalized to the precession period $L_{SO}^{(2D)} = 2\pi v_{SAW}\Omega_{SO}$. The parameters were obtained from fits to Monte-Carlo simulations of the acoustic spin transport along channels with different widths w . Results are shown for transport at 2 K and 10 K under a BIA-type and SIA-type spin-orbit field. The L_{SO} and ℓ_s values were obtained by fitting the calculated spin polarization profiles to Eq. (1) of the main paper.

yield the effective SO length $L_{SO} = \Omega_{SO}/v_{SAW}$ as well as spin decay length ℓ_s (see below). For the widest channel in Fig. SM5, the spin polarization decays with a distance

ℓ_s corresponding roughly to $L_{SO}^{(2D)}$. However, ℓ_s increases significantly with decreasing channel width, as shown in the upper plots of Figs. SM5(b) and SM5(c).

One interesting question is how the spin dynamics depends on the symmetry of the SO interaction. In order to address this question, Fig. SM6 displays spin polarization profiles calculated for different ratios r_s between the SIA and BIA SO contributions. The left and right panels illustrate the momentum dependence of the SO coupling for each of the cases. The calculations were carried out for different channel widths w_y . Figures SM6(a) and SM6(d) are for the pure BIA and SIA contributions, respectively. Within the calculation accuracy, one observes a similar behavior for the two types of asymmetry with the spin decay length ℓ_s increasing with decreasing channel width. Figures SM6(b) and SM6(c) show the simulation results for $r_s = 0.5$ and $r_s = -0.5$, which correspond to the spin helix modes with Ω_{SO} parallel to y and x , respectively (cf. right panels) [24–26]. In both cases, the spin decay reduces significantly.

The dependence of the spin precession period (L_{SO}) and decay lengths obtained from fits of the calculated profiles to Eq. (1) of the main text are summarized in Figs. SM7(a) and (b), respectively. Results are presented for simulations under SIA (filled symbols) and BIA (open symbols) SO fields at the temperatures of 2 K and 10 K, which yield different carrier mean-free-path ℓ_p . The fitted precession periods are found to coincide within 10% with the period $L_{SO}^{(2D)} = 12 \mu m$ quantifying the SO interaction strength in the simulations. Such a behavior is indeed expected from Eqs. (SM18) for $r_s > 0$, when

the magnitude $|\Omega_{\text{SO}}|$ is constant. Since the time Δt for propagation over a short distance $\Delta r = (\Delta x, \Delta y)$, given by $\Delta t = \Delta r/v = m_e^* \Delta r/(\hbar k)$, is inversely proportional to k , then the precession angle around y can be expressed as $\delta\phi = \Omega_{\text{SO}y} \Delta t = \Omega_{\text{SO}} \cos\theta \Delta t = (\hbar/m_e^*) \Omega_{\text{SO}} \Delta x$. As a consequence, the precession period along x does not depend on the spin propagation angle θ .

The dependence of ℓ_s on w_y displayed in Fig. SM7(b) shows two regions with different behaviors. For wide

channels, ℓ_s saturates at a value

$$\ell_s \propto v_{\text{SAW}} * \frac{(L_{\text{SO}}^{(2D)})^2}{2\pi v_y^2 \tau_p}, \quad (\text{SM22})$$

which reduces with increasing temperature. For narrow channels, in contrast, ℓ_s is essentially independent of temperature and increases according to $\ell_s \propto w^{-2}$. Such a dependence agrees with previous simulation results from Refs. 3 and 23 and is attributed to the increased role of motional narrowing for $w_y < L_{\text{SO}}^{(2D)}$.

The results of this section thus show that while the spin precession frequency during acoustic transport is essentially independent of the channel width, the spin decoherence lengths increase significantly in narrow channels ($w_y \ll L_{\text{SO}}$).

-
- [1] B. Baylac, X. Marie, T. Amand, M. Brousseau, J. Barreau, and Y. Shekun, Hole spin relaxation in intrinsic quantum wells, *Surf Sci* **326**, 161 (1995).
 - [2] H. Sanada, T. Sogawa, H. Gotoh, K. Onomitsu, M. Kohda, J. Nitta, and P. V. Santos, Acoustically induced spin-orbit interactions revealed by two-dimensional imaging of spin transport in GaAs, *Phys. Rev. Lett.* **106**, 216602 (2011).
 - [3] A. A. Kiselev and K. W. Kim, Progressive suppression of spin relaxation in two-dimensional channels of finite width, *Phys. Rev. B* **61**, 13115 (2000).
 - [4] A. Hernández-Mínguez, K. Biermann, R. Hey, and P. V. Santos, Spin transport and spin manipulation in (110) and (111) GaAs quantum wells, *Phys. Status Solidi B* **251**, 1736 (2014).
 - [5] M. Z. Maialle, E. A. de Andrada e Silva, and L. J. Sham, Exciton spin dynamics in quantum wells, *Phys. Rev. B* **47**, 15776 (1993).
 - [6] M. I. Dyakonov, V. A. Marushchak, V. I. Perel, M. N. Stepanova, and A. N. Titkov, Spin relaxation of conduction electrons in uniaxial deformed crystal a_3b_5 , *Bull. Acad. Sci. USSR, Phys. Ser.* **47**, 23 (1983).
 - [7] G. E. Pikus, V. A. Marushchak, and A. N. Titkov, Spin splitting of energy bands and spin relaxation of carriers in cubic III-V crystals (review), *Sov. Phys. Semicond.* **22**, 115 (1988).
 - [8] F. Meier and B. P. Zakharchenya, *Optical orientation*, edited by V. M. Agranovich and A. A. Maradudin, Modern problems in condensed matter physics No. 8 (North-Holland, Amsterdam, The Netherlands, 1984).
 - [9] M. Beck, C. Metzner, S. Malzer, and G. H. Doehler, Spin lifetimes and strain-controlled spin precession of drifting electrons in zinc blende type semiconductors, *Europhys. Lett.* **75**, 597 (2006).
 - [10] L. C. Lew Yan Voon and L. R. Ram-Mohan, Tight-binding representation of the optical matrix elements: Theory and applications, *Phys. Rev. B* **47**, 15500 (1993).
 - [11] J. N. Schulman and Y.-C. Chang, Band mixing in semiconductor superlattices, *Phys. Rev. B* **31**, 2056 (1985).
 - [12] M. Cardona, N. E. Christensen, and G. Fasol, Relativistic band structure and spin-orbit splitting of zinc-blende-type semiconductors, *Phys. Rev. B* **38**, 1806 (1988).
 - [13] J. C. Slater and G. F. Koster, Simplified lcao method for the periodic potential problem, *Phys. Rev.* **94**, 1498 (1954).
 - [14] P. V. Santos and M. Cardona, Comment on: Observation of spin precession in GaAs inversion layers using antilocalization, *Phys. Rev. Lett.* **72**, 432 (1994).
 - [15] P. V. Santos, M. Willartzen, M. Cardona, and A. Cantarero, Tight-binding calculations of spin splittings in semiconductor superlattices, *Phys. Rev. B* **51**, 5121 (1995).
 - [16] P. Vogl, H. P. Hjalmarson, and J. D. Dow, A semi-empirical tight-binding theory of the electronic structure of semiconductors, *J. Phys. Chem. Solids* **44**, 365 (1983).
 - [17] K. C. Hass, H. Ehrenreich, and B. Velický, Electronic structure of $\text{Hg}_{1-x}\text{Cd}_x\text{Te}$, *Phys. Rev. B* **27**, 1088 (1983).
 - [18] D. J. Chadi, Spin-orbit splitting in crystalline and compositionally disordered semiconductors, *Phys. Rev. B* **16**, 790 (1977).
 - [19] G. E. Pikus and A. N. Titkov, *Optical orientation* (North Holland, Amsterdam, Amsterdam, 1984) Chap. Spin relaxation under optical orientation in semiconductors, p. 73.
 - [20] M. I. Dyakonov, V. A. Marushchak, V. I. Perel', and A. N. Titkov, The effects of strain on the spin relaxation of conduction electrons in III-V semiconductors, *Sov. Phys. JETP* **63**, 665 (1986).
 - [21] J. A. H. Stotz, R. Hey, P. V. Santos, and K. H. Ploog, Spin transport and manipulation by mobile potential dots in GaAs quantum wells, *Physica E* **32**, 446 (2006).
 - [22] M. M. de Lima, Jr. and P. V. Santos, Modulation of photonic structures by surface acoustic waves, *Rep. Prog. Phys.* **68**, 1639 (2005).
 - [23] A. A. Kiselev and K. W. Kim, Suppression of Dyakonov-Perel spin relaxation in 2d channels of finite width, *physica status solidi (b)* **221**, 491 (2000).
 - [24] B. A. Bernevig, J. Orenstein, and S.-C. Zhang, Exact $\text{SU}(2)$ symmetry and persistent spin helix in a spin-orbit coupled system, *Phys. Rev. Lett.* **97**, 236601 (2006).
 - [25] J. D. Koralek, C. P. Weber, J. Orenstein, B. A. Bernevig, S.-C. Zhang, S. Mack, and D. D. Awschalom, Emergence of the persistent spin helix in semiconductor quantum

- wells, *Nature* **458**, 610 (2009).
- [26] M. P. Walser, C. Reichl, W. Wegscheider, and G. Salis, Direct mapping of the formation of a persistent spin helix, *Nat. Phys.* **8**, 757 (2012).